

## Trends in Downwelling Longwave Radiance over the Southern Great Plains

Lei Liu<sup>1</sup>, Yi Huang<sup>1</sup>, John R. Gyakum<sup>1</sup>, David D. Turner<sup>2</sup>, P. Jonathan Gero<sup>3</sup>

<sup>1</sup>Department of Atmospheric and Oceanic Sciences, McGill University, Quebec, Canada.

<sup>2</sup>NOAA/OAR/Global Systems Laboratory, Boulder, Colorado, USA.

<sup>3</sup>Space Science and Engineering Center, University of Wisconsin-Madison, Madison, Wisconsin, USA.

Corresponding author: Lei Liu ([lei.liu5@mail.mcgill.ca](mailto:lei.liu5@mail.mcgill.ca))

### Key Points:

- Long-term downwelling longwave radiance observations reveal distinctive trends across the infrared spectrum.
- Significant positive radiance trends in weak absorption bands indicate earlier detectability of climate change.
- Radiance trend uncertainty mainly results from natural variability, emphasizing the need to continue the measurements.

This article has been accepted for publication and undergone full peer review but has not been through the copyediting, typesetting, pagination and proofreading process, which may lead to differences between this version and the [Version of Record](#). Please cite this article as [doi: 10.1029/2021JD035949](https://doi.org/10.1029/2021JD035949).

This article is protected by copyright. All rights reserved.

## 18 Abstract

19 Downwelling longwave radiation is an important part of the surface energy budget. Spectral  
20 trends in the downwelling longwave radiance (DLR) provide insight into the radiative drivers  
21 of climate change. In this research, we process and analyze a 23-year DLR record measured  
22 by the Atmospheric Emitted Radiance Interferometer (AERI) at the U.S. Department of  
23 Energy Atmospheric Radiation Program Southern Great Plains (SGP) site. Two AERIs were  
24 deployed at SGP with an overlapping observation period of about 10 years, which allows us  
25 to examine the consistency and accuracy of the measurements and to account for  
26 discrepancies between them due to errors associated with the instruments themselves. We  
27 then analyzed the all-sky radiance trends in DLR, which are associated with the surface  
28 warming trend at SGP during this same period and also the complex changes in  
29 meteorological conditions. For instance, the observed radiance in the CO<sub>2</sub> absorption band  
30 follows closely the near-surface air temperature variations. The significant positive radiance  
31 trends in weak absorption channels, such as in the wings of the CO<sub>2</sub> band and in the weak  
32 absorption channels in the H<sub>2</sub>O vibration-rotational band, show earlier detectability of  
33 climate change. The magnitude of the radiance trend uncertainty in the DLR record mainly  
34 results from internal climate variability rather than from measurement error, which highlights  
35 the importance of continuing the DLR spectral measurements to unambiguously detect and  
36 attribute climate change.

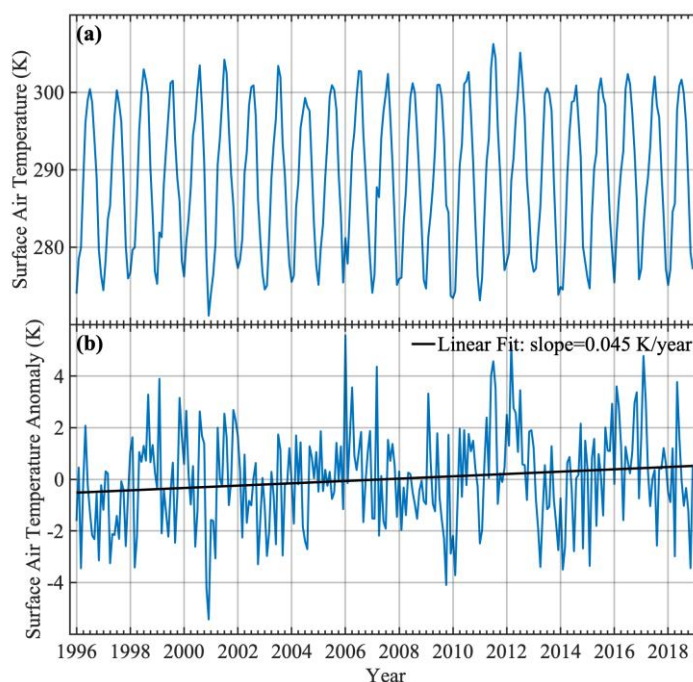
## 37 1 Introduction

38 Longwave radiation is a key component of the atmospheric energy budget that drives  
39 climate change. At the top of the atmosphere (TOA), the outgoing longwave radiation (OLR),  
40 as well as its spectrally resolved radiance, is monitored by satellites with global coverage and  
41 long-term records (e.g., Liebmann & Smith, 1996; Stephens et al., 2012). This allows us to  
42 study changes in OLR and to test climate models (e.g., Brindley & Bantges, 2016; Harries et  
43 al., 2001; Huang & Ramaswamy, 2009; Huang, Ramaswamy, Huang, et al., 2007; Huang,  
44 Ramaswamy, & Soden, 2007; Palchetti et al., 2020; Pan et al., 2015; Wielicki et al., 2002).  
45 Even when there is continuous spatiotemporal coverage of OLR spectra, the compensating  
46 effects of greenhouse gas opacity and temperature warming make it difficult to detect climate  
47 change in satellite measurements (Huang, 2013; Huang & Ramaswamy, 2009).

48 Downwelling longwave radiation emitted by the atmosphere is one key component in  
49 the surface energy budget (Stephens et al., 2012; Trenberth et al., 2009). Compared to the  
50 radiation budget at the TOA, the surface radiation budget is more uncertain and longwave  
51 radiation is a main contributor to the uncertainty (Trenberth et al., 2009; Wild et al., 2012).  
52 This is largely due to the paucity of global and long-term downwelling longwave radiance  
53 (DLR) observations. Despite the limits of spectrally resolved DLR records, it has been  
54 demonstrated that DLR measurements are useful for understanding the surface energy  
55 balance and testing climate models. For example, Lubin (1994) explained the super  
56 greenhouse effect by using observed DLR spectra over equatorial oceans; Feldman et al.  
57 (2015) used the DLR spectra to measure CO<sub>2</sub> radiative forcing at the Southern Great Plains  
58 (SGP) and the North Slope Alaska sites; Shupe and Intrieri (2004), Kapsch et al. (2016),  
59 Huang et al. (2019), Sokolowsky et al. (2020) and several others diagnosed the DLR  
60 variability in relation to sea ice, clouds and other climate changes in polar regions.

61 Climate change is driven by changes in energy balance. This leads us to an  
62 overarching question regarding the surface energy balance: can climate change be detected  
63 and understood by monitoring the DLR spectrum? One advantage of the DLR, compared to  
64 the OLR, is that the compensating effects mentioned earlier vanish. In the DLR, the

65 greenhouse gas opacity and temperature warming effects reinforce each other to increase  
66 DLR. This makes DLR a potentially advantageous observation for monitoring climate change  
67 (Huang, 2013). The signals from different meteorological variables such as temperature,  
68 greenhouse gases, and clouds imprint different spectral signatures. This allows for a spectral  
69 fingerprinting of their changes (Huang et al., 2010). At the SGP site, the fifth generation  
70 European Centre for Medium-Range Weather Forecasts atmospheric reanalysis dataset,  
71 ERA5 (Hersbach et al., 2020), shows that there has been a significant warming in surface air  
72 temperature with a magnitude of  $\sim 0.045$  K/year between 1996 and 2018 (Figure 1). Can this  
73 warming be detected from the DLR spectral records at that site?



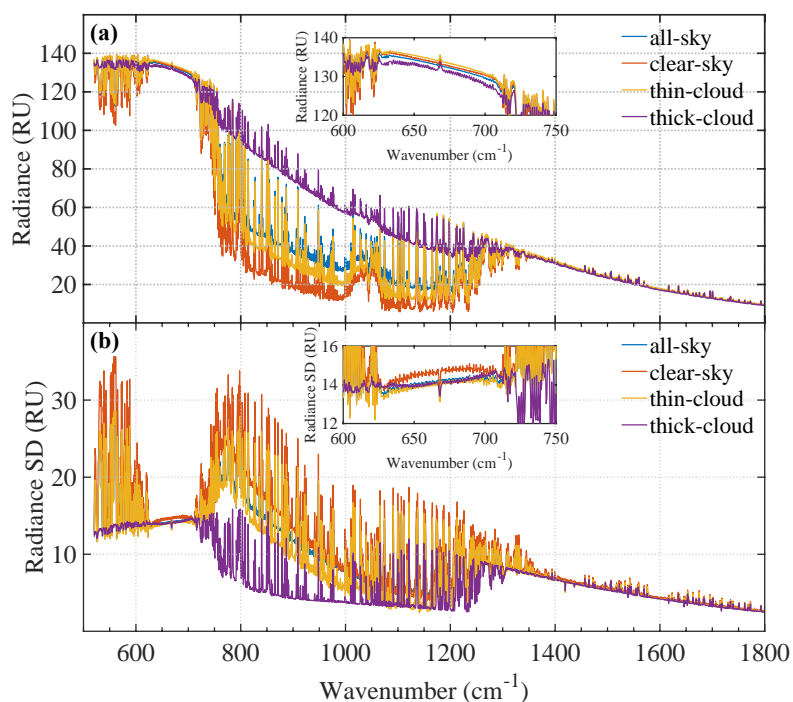
74  
75 **Figure 1.** Warming trend at SGP. Shown here is the ERA5 monthly mean 2-meter air  
76 temperature time series at the SGP site (average of nine  $0.25^\circ \times 0.25^\circ$  resolution grid boxes  
77 centered at:  $97.5^\circ$  W and  $36.5^\circ$  N) between 1996 and 2018. The anomaly is defined with  
78 respect to multi-year monthly mean of each calendar month.

79 We have two primary objectives in this paper. First, we are interested in constructing  
80 a long-term monthly DLR spectral record based on 23 years of measurements by the  
81 Atmospheric Emitted Radiance Interferometers (AERIs) installed at the U.S. Department of  
82 Energy Atmospheric Radiation Measurement (ARM) SGP site. Two AERIs have been  
83 deployed at this site and have rendered 10 years of overlapping observations but with  
84 different sampling strategies (i.e., 3-min sky average every 8 minutes vs multiple 20-s sky  
85 average observations every 4 minutes). We will examine the accuracy and consistency of the  
86 measurements and assess them against synthetic spectra simulated from collocated  
87 atmospheric measurements using a benchmark radiation model. Second, we will analyze the  
88 combined long-term DLR spectral trends for the period of 1996-2018. We are interested in  
89 ascertaining if the radiance trends in the AERI bands dominated by near-surface emission are  
90 consistent with the warming temperature trend shown by ERA5 (Figure 1). This work will  
91 also test the veracity of the trends documented by Gero and Turner (2011) using the early  
92 years of the DLR record and analyze the contributions from different sky conditions.

93 **2 Data and Methods**

## 94 2.1 AERI data processing

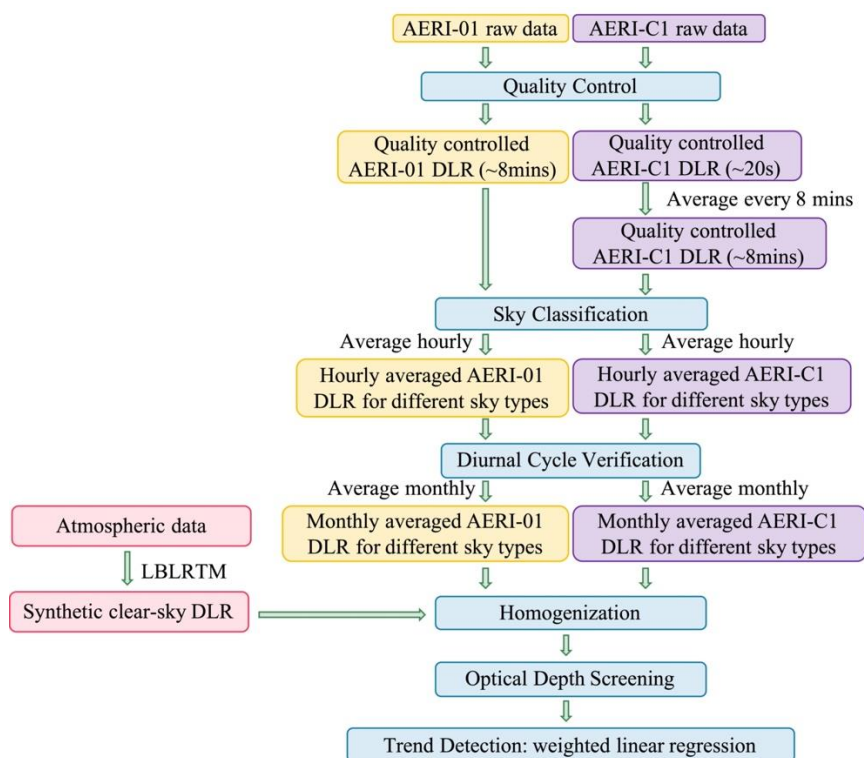
95 The AERI is a ground-based Fourier transform spectrometer that measures the DLR  
 96 emitted from the atmosphere with an accuracy of 1% ambient radiance at high temporal and  
 97 spectral resolution (Knuteson et al., 2004a, 2004b). The measurements cover the spectral  
 98 range between 520 and 3020  $\text{cm}^{-1}$  with a resolution of 0.5  $\text{cm}^{-1}$ ; however, we focus on the  
 99 mid-infrared spectral range from 520 to 1800  $\text{cm}^{-1}$  in this paper. Two high-emissivity  
 100 blackbodies, a hot blackbody with a fixed temperature at 60 degrees Celsius and another  
 101 blackbody at ambient temperature (Knuteson et al., 2004a), are used for radiometric  
 102 calibration based on the method of Revercomb et al. (1988). The long-term average of all 23  
 103 annual mean DLR spectra and the standard deviation of monthly mean DLR spectra over the  
 104 23 years for different sky conditions at the SGP site are shown in Figure 2. We classify the  
 105 scene into three different conditions: clear-sky, thin-cloud, and thick-cloud; the classification  
 106 method will be explained in section 2.2. The main difference in DLR between different sky  
 107 conditions is primarily in the window portion of the spectrum (between 800 – 1200  $\text{cm}^{-1}$ )  
 108 shown in Figure 2a. The standard deviation of thick-cloud DLR is found to be the smallest  
 109 among all the different sky conditions in the window band (Figure 2b), which indicates small  
 110 variability of the radiating temperature of the thick clouds.



111  
 112 **Figure 2.** (a) Long-term average of all 23 annual mean AERI spectra for different sky  
 113 conditions at SGP. (b) Standard deviation of monthly mean AERI spectra for different sky  
 114 conditions at SGP. (RU: Radiance Units; 1 RU = 1  $\text{mW}/(\text{m}^2 \text{sr cm}^{-1})$ ) The insets in the two  
 115 panels indicate the corresponding zoomed-in results in the  $\text{CO}_2$  absorption band.

116 The two AERIs deployed at SGP have different observational periods and different  
 117 sampling frequencies. AERI-01 operated from July 1995 to March 2014, while AERI-C1 has  
 118 operated from February 2004 to the present. C1 is the designator of the Central Facility  
 119 location of the SGP site. Historically E14 was an alternate designator for the same location.  
 120 AERI-C1 was named AERI-E14 before 2011, e.g. in Gero and Turner (2011). The two

121 AERIs were deployed side-by-side (within 5 meters of each other). Given their vertical field  
 122 of view (FOV) of 2.6 degrees full-angle, both instruments view the same portion of the sky;  
 123 86% of the FOVs of the two AERIs are overlapped at the altitude of 1 km. The overlapping  
 124 observations make it possible to test the accuracy and consistency of the measurements.  
 125 However, the two instruments differ with respect to their sampling frequency. AERI-01  
 126 measures one DLR spectrum approximately every 8 minutes; its measurement cycle includes  
 127 a 200-s sky-dwell period (Knuteson et al., 2004b) and the rest of the cycle is used for viewing  
 128 the blackbodies for calibration. AERI-C1 uses a rapid mode with ~20-s sampling cycle  
 129 (Turner et al., 2006). Such differences in the measurements necessitate appropriate  
 130 procedures to homogenize the data from the two AERIs for inter-comparisons and trend  
 131 analyses.



132

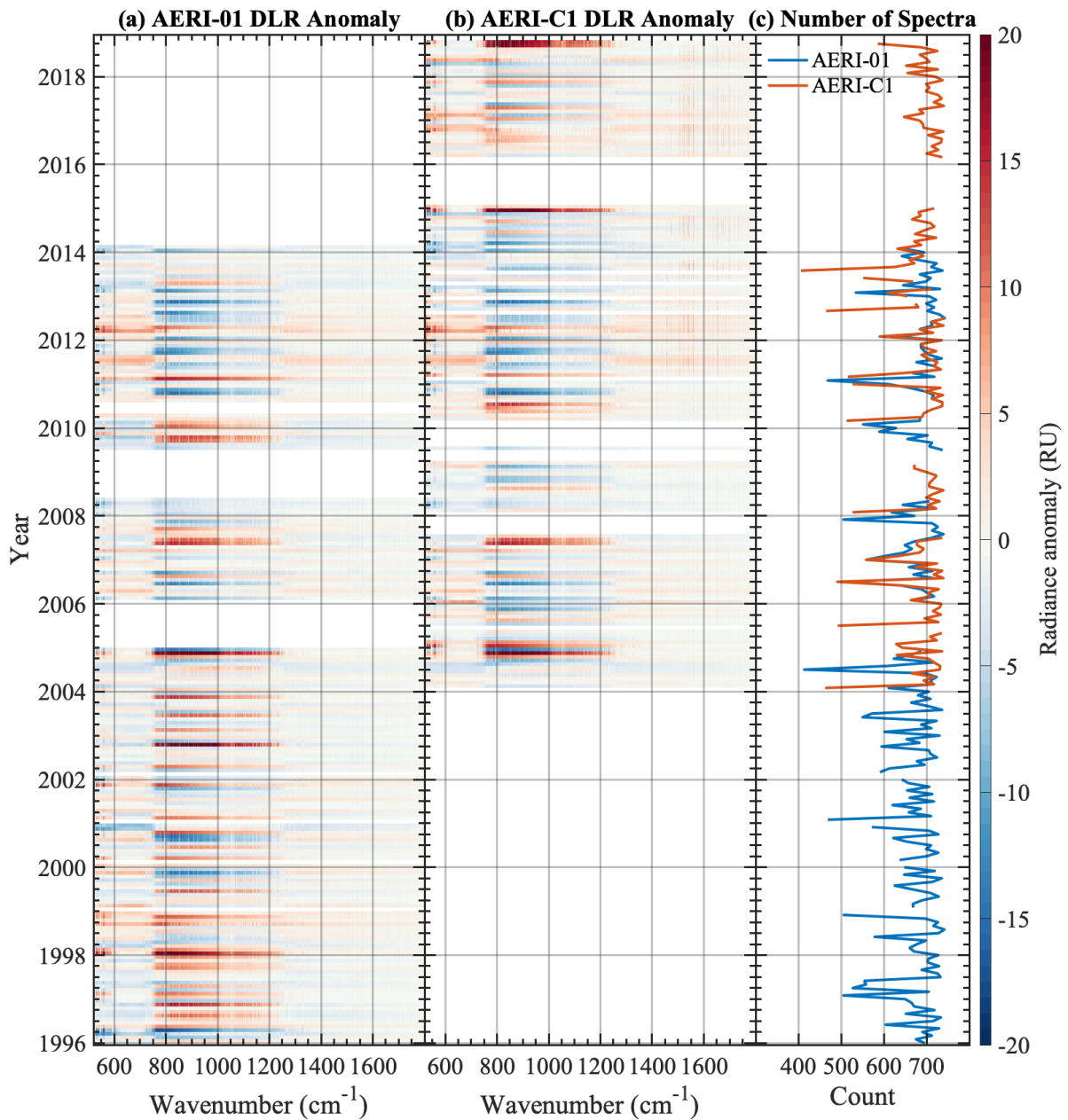
133 **Figure 3.** Data processing flowchart. Yellow and purple squares represent AERI-01 and  
 134 AERI-C1 DLR data respectively. Blue squares represent important data processing steps.  
 135 Pink squares represent radiative transfer model simulations. Details of processing steps are  
 136 provided in the text.

137 Figure 3 shows the flowchart illustrating the data processing adopted in this paper.  
 138 First, rigorous quality control is performed on the data to retain reliable observations. During  
 139 the long history of observations at the SGP site, many factors have caused errors including:  
 140 contamination of the scene mirror, malfunction of the interferometer, and failure of the  
 141 detector temperature sensor. We first discard all the erroneous data based on the AERI  
 142 quality control reports from the ARM program  
 143 ([https://adc.arm.gov/discovery/#/results/instrument\\_class\\_code::aeri](https://adc.arm.gov/discovery/#/results/instrument_class_code::aeri)). In addition, similar to  
 144 the quality control method described in Turner and Gero (2011), the hatch status and the sky  
 145 view noise equivalent radiance tests are also implemented.

146 After the *Quality Control* step, we average the AERI-C1 spectra over 8-min intervals,  
 147 to be consistent with the AERI-01 sampling period. Then, in the *Sky Classification* step, we  
 148 apply a machine learning algorithm (detailed in section 2.2 below) to classify the sky  
 149 conditions as one of clear, thin cloud, or thick cloud overhead based on the 8-min mean

150 radiance spectra. Next, we compute averages of all 8-min spectra of each sky type within  
151 each hour and then average the hourly spectra of the same hour of the day to obtain a  
152 monthly averaged diurnal cycle. It is verified that there is uniform diurnal sampling in each  
153 month; no data of the 24-hour diurnal cycle is missing. Next, the monthly mean spectra are  
154 obtained by averaging the monthly averaged diurnal cycle. Monthly means are discarded  
155 when the count of hourly spectra is below 400 (~ 55%).

156 Some channels in the center of the CO<sub>2</sub> absorption band (~ 667 cm<sup>-1</sup>) and the water  
157 vapor absorption band (1300 – 1800 cm<sup>-1</sup>) for which the near-surface atmosphere is so  
158 opaque that the channels are essentially uncalibrated are discarded in the *Optical Depth*  
159 *Screening* step. These strongly opaque channels are identified using the criterion that the  
160 gaseous optical depth for a 1-meter layer of atmosphere at the surface is above 0.5. Finally,  
161 the monthly-anomaly spectra are obtained by subtracting from each monthly mean spectra  
162 the long-term average of all 23 monthly mean spectra for that calendar month (which  
163 effectively removes the seasonal cycle). These monthly-anomaly time series are illustrated in  
164 Figure 4, and are used in the following analyses and figures. The long-term trends in the DLR  
165 monthly mean spectra are analyzed based on the monthly-anomaly spectra. Synthetic clear-  
166 sky DLR, computed using collocated radiosonde data and a radiative transfer model  
167 (described below), are used as a baseline to evaluate the measurements of the two AERIs  
168 during the overlapping period; details are provided in Appendix A.  
169



170

171

172

**Figure 4.** Monthly anomalies of AERI-observed DLR spectra and hourly spectra count in each month.

173

174

175

176

Both AERIs produced more than 600 hourly mean spectra per month nearly 90% of the time (Figure 4c). The strongest monthly DLR anomalies are seen in the window band (800 – 1200  $\text{cm}^{-1}$ ) (Figure 4a, 4b). The pattern of the DLR anomalies in the overlapping observational period is similar in both AERI-01 and AERI-C1.

177

## 2.2 Sky classification

178

179

180

Clouds strongly influence the DLR spectra, especially in the atmospheric window (800 – 1200  $\text{cm}^{-1}$ ). In order to identify the causes of the DLR trends, we separate the clear-sky spectra from the cloudy cases and examine their trends separately.

181

182

A sky-classification model is developed using a machine-learning method based upon the k-nearest neighbor (k-NN) algorithm (Cunningham & Delany, 2020). The 8-min AERI-

183 01 and AERI-C1 spectra for the period between 1 March 2011 and 31 July 2012 are used to  
184 train the k-NN model. We use the same inputs and truth data from Raman Lidar as in Turner  
185 and Gero (2011). The k-NN classification achieves an accuracy of 94.8%. This algorithm  
186 determines the sky to be *clear* or *cloudy*, while the cloudy sky is then further classified to be  
187 *thin-cloud* when 70-minute averaged  $985\text{ cm}^{-1}$  brightness temperature is lower than 250K;  
188 otherwise, it is classified to be *thick-cloud*. We also tried a classical backpropagation  
189 gradient-descent classification algorithm as used by Turner and Gero (2011), which achieves  
190 an accuracy of 90%. The resulting trends are not sensitive to the classification method  
191 chosen. The results presented below are based on the k-NN algorithm.

192 Based on the classification of *thin-cloud* and *thick-cloud*, the *thick-cloud* emitting  
193 temperature range is smaller than that for *thin-cloud*, primarily because *thick-clouds* are  
194 opaque clouds relatively close to the surface while *thin-cloud* may be either partially cloudy  
195 scenes or clouds higher in the troposphere. This is why the *thick-cloud* classification has the  
196 smallest standard deviation of DLR among the three different sky conditions.

### 197 2.3 Homogenization

198 During the overlapping observational period, discrepancies larger than the  
199 documented AERI absolute calibration uncertainty (Knuteson et al., 2004a) were observed  
200 between the monthly mean spectra observed by AERI-01 and AERI-C1. Large radiance  
201 discrepancies occur, especially in the window band, and are found to mainly come from  
202 clear-sky scenes (see Figure B1 and discussions in Appendix B). This suggests that the  
203 discrepancies likely result from calibration (Rowe, Neshyba, Cox, et al., 2011; Rowe,  
204 Neshyba, & Walden, 2011) and other undetected errors (e.g., something in the FOV of one  
205 instrument but not the other). In order to avoid discarding meaningful data in the trend  
206 analysis, we simulate the clear-sky DLR spectra using a radiation model together with  
207 collocated atmospheric measurements and use these synthetic spectra as a reference to assign  
208 proper weights in combining the data of AERI-01 and AERI-C1, based on the findings of  
209 previous radiance closure studies (e.g., Turner et al., 2004) that demonstrated high accuracy  
210 in such synthetic spectra.

211 The radiation model used here is the Line-by-Line Radiative Transfer Model  
212 (LBLRTM v12.9) (Clough et al., 2005). To compute the clear-sky DLR spectra at SGP, we  
213 use the temperature and water vapor profiles from the ARM Balloon-Borne Sounding System  
214 (<https://www.arm.gov/capabilities/instruments/sonde>). The water vapor mixing ratio profiles  
215 derived from radiosondes are scaled with a height-independent factor to match the  
216 precipitable water vapor retrieved by the microwave radiometer at the SGP site. This  
217 approach has been used to compensate for the dry-bias issue found in the radiosonde water  
218 vapor data (Holdridge, 2020; Revercomb et al., 2003; Turner et al., 2003; Wang et al., 2002).  
219 CO<sub>2</sub> and CH<sub>4</sub> concentration profiles are obtained from the CarbonTracker website  
220 (<http://carbontracker.noaa.gov>, Jacobson et al., 2020; Peters et al., 2007). O<sub>3</sub> concentration  
221 profiles are adjusted from NASA's Modern-Era Retrospective analysis for Research and  
222 Applications, Version 2 (MERRA-2, Gelaro et al., 2017) ozone product to get a better  
223 radiative closure with AERI-observed DLR (see more details in Appendix B). We use a 200-  
224 level input profile for the LBLRTM simulations. The first and second levels are at 0m and  
225 10m above ground level respectively. The depth of each subsequent layer is increased by 2%  
226 relative to the one below.

227 As radiosonde observations of near-surface layers are essential to the DLR spectra,  
228 the AERI data are selected to match the radiosonde launch time. We keep the spectra whose  
229 observation time is within 10 minutes of the radiosonde launch time. For each month, about



230 70 clear-sky DLR spectra are simulated on average. The absolute values of the radiance  
 231 biases ( $R_{bias}$ ) are determined as the monthly mean radiance differences between the synthetic  
 232 and observed DLR spectra.

233 During the overlapping observational period, the monthly mean AERI-01 and AERI-  
 234 C1 DLR spectra are combined according to Equation (1) and Equation (2) using the ratio  $r$ ,  
 235 which represents the proximity of the AERI's observed DLR spectra to the synthetic DLR  
 236 spectra.  $r$  is a function of wavenumber. The 5<sup>th</sup>, 50<sup>th</sup> and 95<sup>th</sup> percentiles of the ratio  $r$  across  
 237 all AERI channels over the 23-year period are 0.55, 2.06, and 12.84 respectively. The  
 238 weighted radiance used in the trend analysis is given by Equation (2), where  $R_{AERI-01}$  and  
 239  $R_{AERI-C1}$  represent the observed AERI-01 and AERI-C1 monthly mean DLR respectively.

$$240 \quad r = \frac{R_{bias(AERI-01-LBLRTM)}}{R_{bias(AERI-C1-LBLRTM)}} \quad (1)$$

$$241 \quad R = R_{AERI-01} \times \frac{1}{1+r} + R_{AERI-C1} \times \frac{r}{1+r} \quad (2)$$

#### 242 2.4 Trend detection

243 A weighted linear regression method is applied to determine if there are any trends in  
 244 the observed DLR. We develop our weighted linear regression model based on the regression  
 245 model developed by Tiao et al. (1990) and Weatherhead et al. (1998).

246 This model determines the radiance trend,  $\hat{\omega}$ , in each AERI channel, as:

$$247 \quad \hat{\omega} = \frac{\sum_{t=1}^T W_t (t - \bar{t}) y_t^*}{\frac{1-\phi}{12} \sum_{t=1}^T W_t (t - \bar{t})^2} \quad (3)$$

248 In Equation (3),  $T$  represents the total number of months and  $\bar{t}$  represents the mean  
 249 value of  $t$ .  $\phi$  is the autocorrelation in the noise of the time series considering a first-order  
 250 autoregressive (AR1) process, and  $y_t^*$  represents the transformed radiance anomalies (see  
 251 Figure A1) after removing the effect of the AR1 process (see details in Appendix A).  $W_t$   
 252 represents the weights which are determined as the intra-month variability of the all-sky  
 253 observed DLR, shown in Equation (4):

$$254 \quad W_t = \frac{N_t}{\sigma_t^2} \quad (4)$$

255 where  $N_t$  and  $\sigma_t^2$  represent the number and variance of hourly observations in each month.  
 256 Large variability of DLR results in smaller weights. We use the same weights for all sky  
 257 conditions.

258 Along with the magnitude of the trend it is also important to determine the associated  
 259 uncertainty,  $\sigma_{\hat{\omega}}$ , which is shown in Equation (5). In Equation (5),  $\sigma_N^2$  and  $\sigma_e^2$  represent the  
 260 variance of the error due to internal variability in the time series and the variance of the  
 261 measurement error respectively. Here, we mainly account for two sources of uncertainty.  
 262 First, there is the uncertainty arising from internal climate variability. This is accounted for  
 263 by the term in Equation (5) associated with  $\sigma_N$  and  $\phi$ . Second, there is the uncertainty arising  
 264 from instrumentation errors accounted for by the term in Equation (5) associated with  $\sigma_e$ . We  
 265 use the radiance difference between clear-sky LBLRTM simulation and clear-sky AERI-  
 266 observation as the measurement error. We assume that these two sources of uncertainty are  
 267 independent of each other. The derivation of Equation (5) is given in Appendix A.

268

$$\sigma_{\hat{\omega}} = \frac{12 \sqrt{\sum_{t=1}^T W_t^2 (t - \bar{t})^2}}{\sum_{t=1}^T W_t (t - \bar{t})^2} \sqrt{\sigma_N^2 \frac{1 + \phi}{1 - \phi} + \sigma_e^2} \quad (5)$$

269

270

271

272

273

The derived  $\sigma_{\hat{\omega}}$  in Equation (5) is referred to as the standard error of the trend magnitude. It is used to test whether the trends deviate significantly from 0 at the 95% significance level. A trend is considered to be significant at the 95% significance level if the trend magnitude is larger than  $2\sigma_{\hat{\omega}}$ . In following figures, the uncertainty envelope plotted in gray corresponds to the 95% confidence interval.

### 274 3 Results

#### 275 3.1 All-sky radiance trends

276

277

278

The homogenized DLR records have been constructed, based on monthly averaged AERI-01 data from 1996 to 2013 and AERI-C1 data from 2004 to 2018. In total, we have 23 years of DLR data at SGP for analysis.

279

280

281

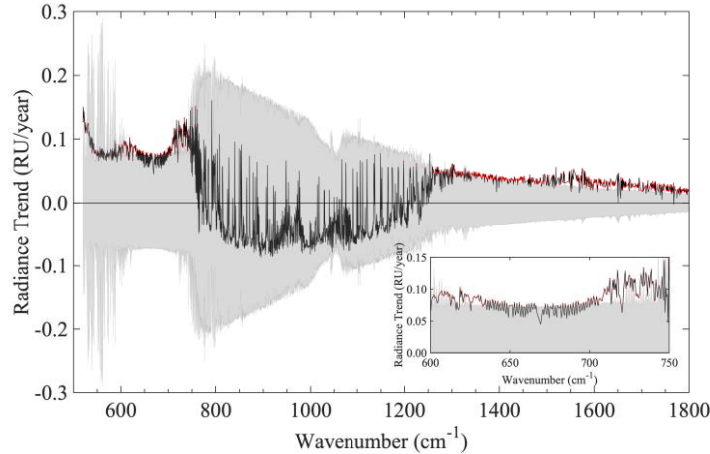
282

283

284

285

It can be inferred from the monthly anomalies shown in Figure 4 that the DLR trends depend on the analysis period as the anomalies do not show monotonic changes over this 23-year period. The AERI-01 data (Figure 4a) show more frequent negative anomalies after 2011 in the window band (800-1200  $\text{cm}^{-1}$ ), which is consistent with the negative trends reported in Gero and Turner (2011) for this instrument. However, including AERI-C1 data (Figure 4b) affords a longer DLR spectral record, and the latest several years are characterized by warm anomalies.



286

287

288

289

**Figure 5.** The all-sky radiance trends. The spectral elements indicated with red dots have trends that exceed the 95% significant test. The shading in the figure is the 95% confidence interval. The inset shows the zoomed-in results of CO<sub>2</sub> absorption band.

290

291

292

293

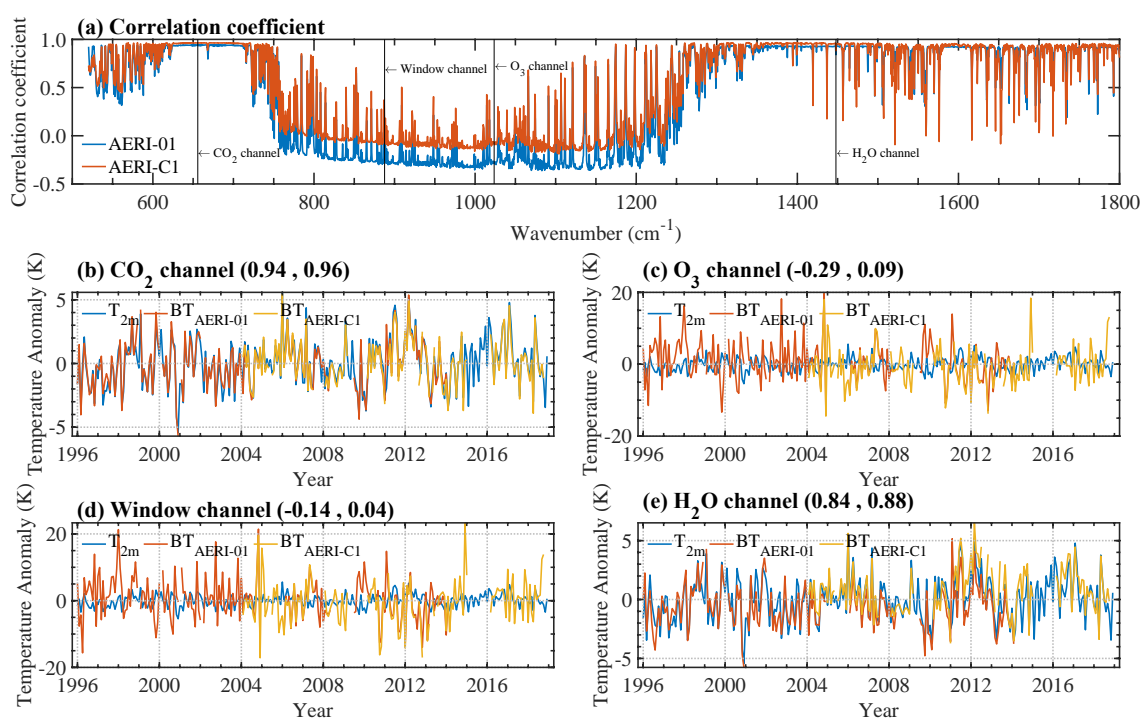
294

295

296

The long-term all-sky radiance trends during the 1996-2018 period are shown in Figure 5. The all-sky DLR trends have different features in different spectral regions. In the CO<sub>2</sub> absorption band centered around 667  $\text{cm}^{-1}$ , the trends are generally positive (i.e., radiance is increasing over time) and are statistically significant in the band wings but not at the center. In the window band (800-1200  $\text{cm}^{-1}$ ), there are very few statistically significant trends. In the water vapor absorption band (1300-1800  $\text{cm}^{-1}$ ), similar to the CO<sub>2</sub> absorption band, the radiance trends are generally positive and statistically significant.

297 DLR in different AERI channels are controlled by different meteorological variables.  
 298 To illustrate this point, Figure 6a shows the correlation coefficients between the  
 299 deseasonalized and detrended monthly anomalies in the radiance (brightness temperature)  
 300 spectra from the two AERIs and surface air temperature from ERA5. Note that AERI-01 and  
 301 AERI-C1 have different observational periods, which result in different correlation  
 302 coefficients especially in the window band. In the center of the CO<sub>2</sub> absorption band (667 cm<sup>-1</sup>)  
 303 and channels corresponding to strong H<sub>2</sub>O absorption lines, the correlation coefficient is  
 304 close to one, indicating that the variance in the radiance in these channels is primarily  
 305 controlled by the surface air temperature. This is because the atmospheric absorption is  
 306 strongly saturated in these channels and thus they are less sensitive to variations in the  
 307 concentrations of the gases themselves and to temperatures of the atmospheric constituents  
 308 farther removed from the surface. In comparison, in the wings of the CO<sub>2</sub> band and the  
 309 weaker H<sub>2</sub>O absorption lines, the atmospheric absorption is not saturated so that variability in  
 310 DLR is subject to the variation in the temperature and gas concentration throughout the  
 311 vertical column. This means that the trends both in temperature and gas concentrations drive  
 312 the radiance to increase, which explains the stronger and statistically more significant trend  
 313 signals in these channels, as seen in Figure 5.



314  
 315 **Figure 6.** (a) The correlation coefficient between the AERI-observed brightness temperature  
 316 spectra and near-surface air temperature from ERA5 at the SGP site over the 23-year period.  
 317 (b-e) The time series of the deseasonalized brightness temperature and near surface air  
 318 temperature in four AERI channels. In each title, the values in the parentheses are the  
 319 correlation coefficients between near-surface air temperature from ERA5 and observed  
 320 brightness temperature by AERI-01 and AERI-C1, respectively.

321 In Figure 6, the time series of the brightness temperature in four selected AERI  
 322 channels: a CO<sub>2</sub> channel at 655.72 cm<sup>-1</sup>, a window channel at 887.63 cm<sup>-1</sup>, a O<sub>3</sub> channel at  
 323 1023.60 cm<sup>-1</sup>, and a H<sub>2</sub>O channel at 1447.89 cm<sup>-1</sup> (Figures 6b to 6e) are displayed. There is  
 324 good consistency between the AERI-01 and AERI-C1 observed brightness temperature in all  
 325 four channels. The all-sky brightness temperature at the CO<sub>2</sub> channel follows closely with the  
 326 surface air temperature from ERA5 (Figure 6b). The near-surface warming of 0.045 K/year

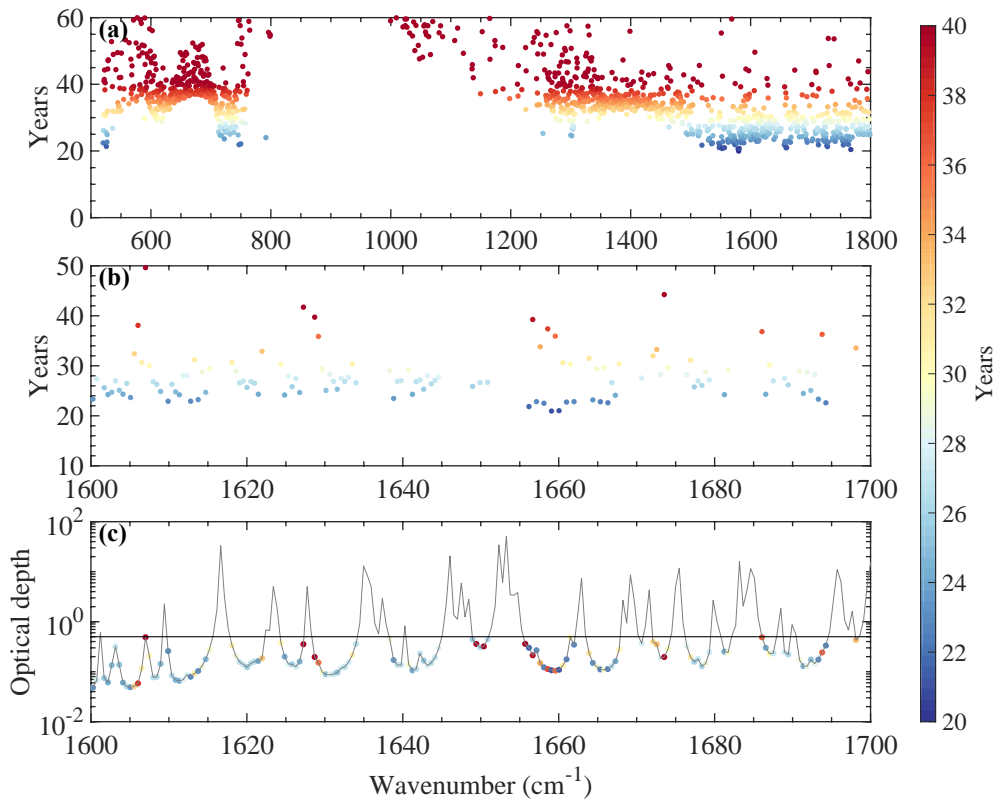
327 (Figure 1) is equivalent to 0.071 RU/year at this channel, which is close to the observed all-  
 328 sky radiance trend of  $\sim 0.072$  RU/year (averaged trend between 5 nearby channels). In the  
 329 H<sub>2</sub>O channel, the brightness temperature measured by the AERIs also follows the near  
 330 surface air temperature (Figure 6e) but not as closely as the CO<sub>2</sub> channel (Figure 6b). In  
 331 contrast, the brightness temperature anomalies in the window and O<sub>3</sub> channels have larger  
 332 fluctuations than that in the CO<sub>2</sub> and H<sub>2</sub>O channels and are evidently decoupled from the near  
 333 surface air temperature (Figure 6c and 6d).

334 That the radiance trend is reinforced by both warming and opacity effects in the weak  
 335 absorption channels indicates the benefits of using these AERI measurements in climate  
 336 change detection. Assuming the trend magnitude and uncertainty determined from this 23-  
 337 year record remain unchanged into future, the years to detect a significant trend,  $n^*$ , at 90%  
 338 significance level is:

$$339 \quad n^* \approx \frac{3.3\sigma_{\hat{\omega}}}{|\hat{\omega}|} \times 23 \text{ years} \quad (6)$$

340 where  $\hat{\omega}$  is the 23-year trend determined by Equation (3) and  $\sigma_{\hat{\omega}}$  is the trend  
 341 uncertainty determined by Equation (5). The derivation of Equation (6) is given in Appendix  
 342 A.4. Although the trends are considered significant when  $|\hat{\omega}| > 2\sigma_{\hat{\omega}}$ , we require  $|\hat{\omega}| >$   
 343  $3.3\sigma_{\hat{\omega}}$  when computing  $n^*$ . As discussed in Appendix C, this yields a more conservative  
 344 estimation of  $n^*$  compared to the method of Leroy et al. (2008).

345 Based on this equation, approximately 30 years are needed to detect a significant  
 346 trend in the 2-meter air temperature from the ERA5 data shown in Figure 1 when  $\hat{\omega}$  and  $\sigma_{\hat{\omega}}$   
 347 are substituted with the 2-meter air temperature trend magnitude and trend uncertainty,  
 348 respectively. In comparison, Figure 7 shows earlier detectability of the radiance trends in  
 349 weak absorption channels, such as in the wings of the CO<sub>2</sub> band and in the weak absorption  
 350 channels in the H<sub>2</sub>O vibration-rotational band. In Figure 7c, the earlier detectability of the  
 351 radiance trends in the H<sub>2</sub>O vibration-rotational band is noticeable in the wings of strong  
 352 absorption lines (i.e., where the optical depth is relatively lower). We can conclude that it is  
 353 advantageous to monitor the DLR in these weaker-absorption channels for climate change  
 354 detection.



355

356 **Figure 7.** Trend detectability. (a) Time to detect (T2D) radiance trends at 90% significance  
 357 level in different AERI channels; in comparison, the T2D for the 2-meter temperature from  
 358 the ERA5 reanalysis is about 30 years. (b) Zoomed-in figure of panel (a) in the water vapor  
 359 absorption band. (c) The T2D (color-coded), in relation to atmospheric absorption strength,  
 360 measured by the optical depth of a 1-meter-thick atmospheric layer near the surface. The  
 361 horizontal line marks optical depth of 0.5.

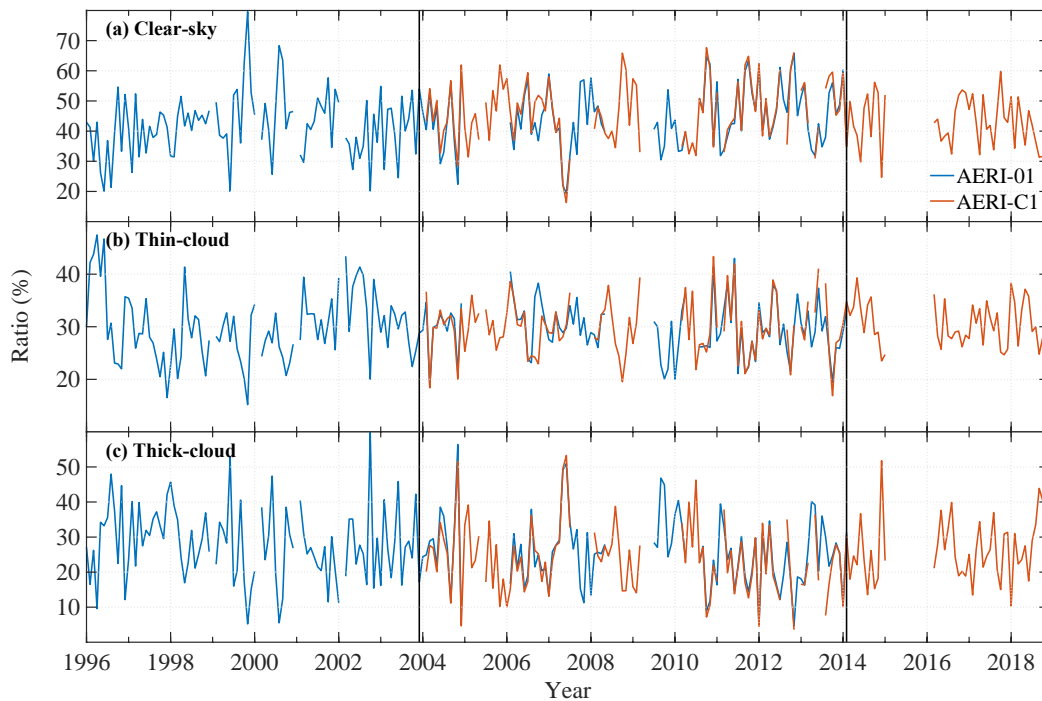
362 Trend detection in the radiance record is determined by comparing the trend signal to  
 363 the uncertainties arising from different causes. Here, based on Equation (5), we account for  
 364 uncertainties arising from climate internal variability ( $\sigma_N$ ) and also instrumentation error ( $\sigma_e$ )  
 365 (Figure 5). The overall uncertainty is notably large in the window band for the all-sky  
 366 condition (Figure 5), which impedes the detection of any significant radiance trends in this  
 367 especially variable spectral region. Analysis of the respective parameters in Appendix A (see  
 368 Figure A2) indicates that internal climate variability dominates instrumentation error when  
 369 shaping the overall uncertainty envelope in Figure 5. It is also found that the influence of the  
 370 autoregressive process does not strongly influence the trend uncertainty, as evident by the  
 371 small value of  $\phi$ , especially in the window band (Figure A2). We conclude that the trend  
 372 uncertainty mainly arises from internal climate variability.

### 373 3.2 Trends in different cloud conditions

374 The results presented in the previous subsection demonstrate that the radiance trends  
 375 in the window band are different from the greenhouse gas absorption bands; the window  
 376 band is also prone to high levels of uncertainty due to the marked variability of the signal that  
 377 ranges from small values in clear sky conditions to large values when opaque low-altitude  
 378 clouds are overhead. Given the fact that clouds are a significant factor that influences this  
 379 band (see Figure 2), we analyze the radiance trends under different cloud conditions in this  
 380 subsection.

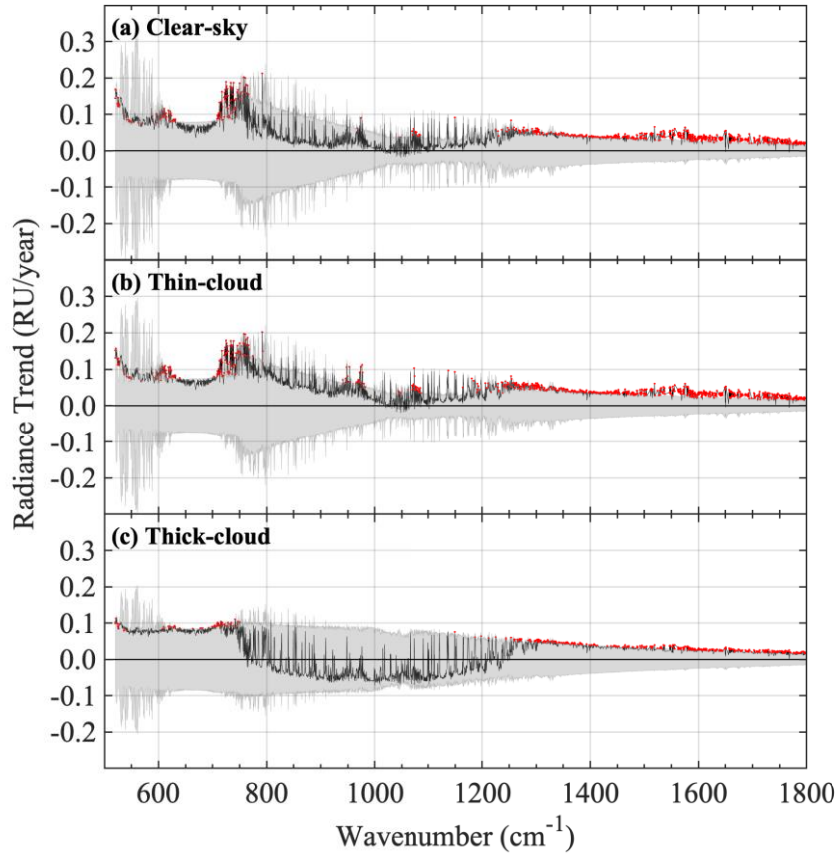
381 The fraction of time that each sky condition occurs in one month (referred to as ‘sky  
 382 fraction’) based on the hourly spectra are shown in Figure 8. First, there is a good agreement  
 383 between AERI-01 and AERI-C1 in the sky fraction monthly time series, with correlation  
 384 coefficients of 0.94, 0.89, and 0.94 for clear-sky, thin-cloud, and thick-cloud, respectively.  
 385 The clear-sky fraction between June 1996 and May 2010 from our classification is around  
 386 42% which is comparable to what was found by Turner and Gero (2011).

387 The clear-sky fraction increases at a rate of  $0.17 \pm 0.09$  % per year, while the thick-  
 388 cloud fraction decreases at a rate of  $-0.18 \pm 0.09$  % per year. There is no significant trend for  
 389 thin-cloud fraction. Understanding the atmospheric mechanisms that drive the trends in the  
 390 sky fraction for different sky conditions are the subject of investigation in a future work.



391  
 392 **Figure 8.** The monthly sky fractions of different sky conditions, categorized based on 8-  
 393 minute mean spectra at the SGP site. The overlapping observational period is between the  
 394 two vertical thick black lines.

395 Trends in AERI-observed DLR for different sky conditions based on the k-NN  
 396 classifier are shown in Figure 9. In the window band, the clear-sky and thin-cloud trends are  
 397 positive, while the thick-cloud trends are negative; however, none of those trends are  
 398 statistically significant from zero because of the notably large trend uncertainty. The positive  
 399 trend in the window band in the clear-sky data is likely due to increases in precipitable water  
 400 vapor (PWV), as hypothesized by Gero and Turner (2011). The positive trend in the thin-  
 401 cloud classification suggests that either the clouds in these scenes are becoming more opaque,  
 402 the clouds are becoming warmer (perhaps by moving lower in the troposphere), the PWV is  
 403 increasing, or some combination of the three. The decrease in the thick-cloud trend in the  
 404 window suggests that these thicker clouds are either becoming cooler or moving higher in the  
 405 troposphere. In the spectral regions outside the window band, the trends for different sky  
 406 conditions are generally positive and have the same features as the all-sky scenes.



407

408 **Figure 9.** The trends in AERI-observed DLR for different sky conditions at the SGP site. The  
 409 spectral elements marked with red dots indicate that the trends pass the 95% significance test.  
 410 The shading in the figure is the 95% confidence interval.

411 The all-sky DLR trends are caused by changes in both sky fraction and the radiance of  
 412 each sky condition. We use equation (7) to separate the contributions from these factors, in  
 413 which  $R_{all}$  represents the all-sky radiance,  $f_i$  and  $R_i$  represent the sky fraction and mean  
 414 radiance for different sky conditions.

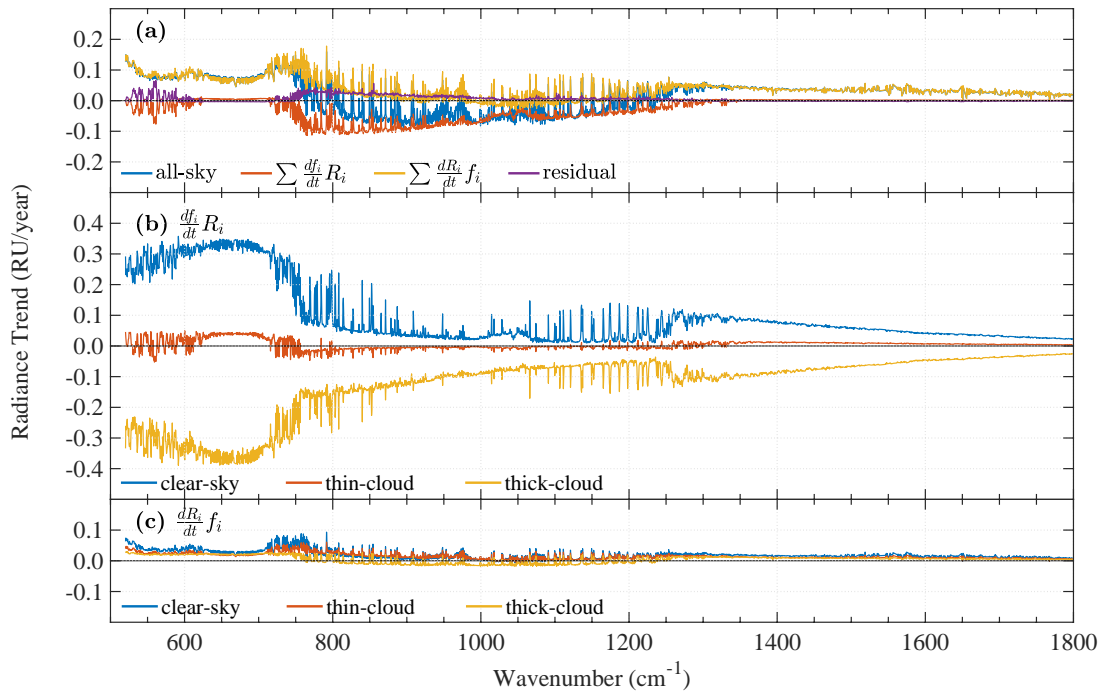
$$415 \quad \frac{dR_{all}}{dt} = \sum \frac{df_i}{dt} R_i + \sum \frac{dR_i}{dt} f_i + residual \quad (7)$$

416 The results of the decomposed trends based on Equation (7) are shown in Figure 10.  
 417 The small residual term (purple line in Figure 10a), which comes from nonlinear effects,  
 418 suggests that the overall all-sky radiance trends can be well explained by Equation (7). In the  
 419 window band, the overall radiance trends are a result of the compensation between the sky  
 420 fraction change (orange line in Figure 10a) and the radiance change (yellow line in Figure  
 421 10a). In the opaque portions of the CO<sub>2</sub> absorption band (centered at 667 cm<sup>-1</sup>) and H<sub>2</sub>O  
 422 absorption band (1300 – 1800 cm<sup>-1</sup>), the overall radiance trends are caused by radiance  
 423 change which is due almost entirely to the increases in the near-surface temperature because  
 424 the atmosphere is already too opaque to reflect any gas concentration changes.

425 The overall radiance trends caused by sky fraction changes (orange line in Figure 10a)  
 426 are a result of the compensation between changes in the clear-sky (blue line in Figure 10b)  
 427 and the thick-cloud fraction (yellow line in Figure 10b) except in the opaque regions of the  
 428 CO<sub>2</sub> absorption band (centered at 667 cm<sup>-1</sup>) and H<sub>2</sub>O absorption band (1300 – 1800 cm<sup>-1</sup>). In  
 429 the CO<sub>2</sub> absorption band and H<sub>2</sub>O absorption band, the perfect compensation between  
 430 positive trends caused by clear-sky and thin-cloud sky fraction changes and the negative

431 trends caused by thick-cloud sky fraction changes results in almost no trends. In the window  
 432 band, the negative trends are mainly caused by the thick-cloud fraction change.

433 In the window band (800 -1200  $\text{cm}^{-1}$ ), the overall radiance trends caused by radiance  
 434 change (yellow line in Figure 10a) result from the compensation between positive clear-sky  
 435 and thin-cloud radiance change trends and negative thick-cloud sky radiance change trends  
 436 (Figure 10c). By contrast, in the  $\text{CO}_2$  absorption band (centered at 667  $\text{cm}^{-1}$ ) and  $\text{H}_2\text{O}$   
 437 absorption band (1300 – 1800  $\text{cm}^{-1}$ ), the radiance changes for the three sky conditions all  
 438 contribute similarly to the overall radiance trends caused by radiance change.



439

440 **Figure 10.** The all-sky DLR trends decomposed into the contributions from the sky fraction  
 441 and radiance changes of different sky conditions. (a) The blue line represents the calculated  
 442 all-sky DLR trends, which is the same as that from Figure 5. The orange and yellow lines  
 443 represent the contribution from sky fraction change and radiance change determined using  
 444 equation (7), respectively. The purple line is the residual term from Equation (7); (b) The all-  
 445 sky DLR trends caused by sky fraction change. The blue, orange, and yellow lines represent  
 446 the contributions from clear-sky, thin-cloud, and thick-cloud fraction changes respectively;  
 447 (c) The all-sky DLR trends caused by radiance change. The blue, orange, and yellow lines  
 448 represent the contributions from clear-sky, thin-cloud, and thick-cloud radiance changes  
 449 respectively.

#### 450 4 Discussion and Conclusions

451 In this study, a long-term record of DLR at the SGP site has been constructed for  
 452 analyzing the DLR trends, based on a weighted linear regression method that takes into  
 453 account both natural climate variability and measurement error. Compared to previous  
 454 studies, our analysis is based on a longer DLR record combined from the two AERIs at the  
 455 SGP site, and makes use of synthetic DLR data in validating and differentiating the AERI  
 456 measurements over their overlapping observational period. In addition, we quantitatively  
 457 decompose the overall radiance trends due to the contributions from sky fraction change and  
 458 the radiance change in each of these sky conditions.



459 The trends in DLR in different spectral ranges have different features. The trends are  
460 generally positive in the CO<sub>2</sub> and H<sub>2</sub>O absorption bands, while no statistically significant  
461 trends are detected in the window band (Figure 5). We find that in the more opaque regions  
462 in the center of the CO<sub>2</sub> and H<sub>2</sub>O absorption bands, the radiance is controlled by the near-  
463 surface air temperature (Figure 6) because of the strong atmospheric absorption. The  
464 sensitivity of DLR to near-surface air temperature indicates the potential of DLR to monitor  
465 climate change. In the wings of these absorption bands, both the near-surface atmospheric  
466 warming and the increase of the abundance of these trace gases contribute to the radiance  
467 trends (Feldman et al., 2015), which makes a climate trend signal more readily detectable, as  
468 hypothesized by Huang (2013). In the window band, the radiance is decoupled from the near-  
469 surface air temperature (Figure 6) because of the impact of sky-fraction changes of different  
470 scenes (clear and cloudy-skies).

471 We find that the sky-fraction change and the radiance change led to compensating  
472 effects on the DLR trends. This compensation results in weakly (statistically insignificant)  
473 negative radiance trends in the window band (Figure 10). In contrast, the radiance trends are  
474 dominated by the radiance change in the CO<sub>2</sub> and H<sub>2</sub>O absorption bands, which are similar in  
475 all three sky conditions.

476 The influences of both natural climate variability and measurement error are  
477 considered when determining the uncertainty of the trend magnitude (Equation (5), Figure  
478 A2). We find that for all sky conditions, the majority of the uncertainty comes from the  
479 natural variability. This underlines the necessity of continuous DLR measurements to  
480 ascertain the DLR trends, especially in the window band (Figure 5).

481 The two AERIs at the SGP site provide us with an excellent opportunity to test the  
482 accuracy and consistency of the instruments. The discrepancies between the two AERIs in  
483 the overlapping periods may have come from calibration error and other undetected  
484 instrumentation errors. In this study, we use synthetic data to differentiate and combine the  
485 two AERIs' observations. Further investigation is required to understand the origin of the  
486 discrepancies and therefore to assure the measurement accuracy.

487 This paper has focused on the detection, as opposed to attribution, of the DLR trends.  
488 In the clear-sky case, atmospheric temperature and radiative gas concentration changes  
489 (primarily water vapor) are likely the main contributors to the DLR changes. As for the  
490 cloudy-sky case, changes in both the atmospheric states and cloud properties may contribute  
491 to the DLR changes. Future work is warranted to understand and quantitatively attribute the  
492 DLR trends disclosed in this paper to different meteorological variables.

#### 493 494 **Acknowledgments**

495 This work is supported by grants from the Fonds de Recherche Nature et Technologies of  
496 Quebec (PR-283823) and the Canadian Space Agency (19FAMCGB16). We would like to  
497 thank John Brown of NOAA GSL for comments on an earlier version of this manuscript and  
498 Lucas Vargas Zeppetello and two anonymous reviewers for their constructive review  
499 comments. LL acknowledges the support of a Dr. and Mrs. Milton Leong Graduate  
500 Fellowship of McGill University. The original AERI data can be obtained from the ARM  
501 data repository (<http://www.arm.gov>). Our processed monthly mean AERI spectra are  
502 available from Mendeley Data (<https://data.mendeley.com/datasets/hdwfm3zpd8/2>).  
503 CarbonTracker CT2019B results are provided by NOAA GML, Boulder, Colorado, USA  
504 from the website at <http://carbontracker.noaa.gov>. CarbonTracker-CH<sub>4</sub> results are provided  
505 by NOAA ESRL, Boulder, Colorado, USA from the website at  
506 <http://www.esrl.noaa.gov/gmd/ccgg/carbontracker-ch4/>.

507  
508  
509

## Appendix A: Trend Detection

510 We first summarize the linear trend model and trend estimation from Tiao et al.  
511 (1990) and Weatherhead et al. (1998) in A.1 and A.2. We adopt the notation in their papers.  
512 Then we add the measurement error term to the trend detection in A.3 following Tiao et al.  
513 (1990).

### 514 A.1 Basic linear trend modeling

515 In order to detect a linear trend, we first construct a simple model that describes the  
516 monthly mean radiance  $Y_t$  as:

$$517 \quad Y_t = \mu + S_t + \omega X_t + N_t, t = 1, \dots, T \quad (A1)$$

518 where  $\mu$  is a constant term,  $S_t$  represents the seasonal component,  $\omega$  is the trend magnitude to  
519 be determined,  $X_t = \frac{t}{12}$  represents time measured in the units of year,  $N_t$  represents the  
520 unexplained portion of the data (i.e. the noise), and  $T$  represents the length of the data set in  
521 months.

522 The seasonal component  $S_t$  is determined by computing a long-term average of each  
523 calendar month. This component is subsequently removed from the monthly mean.

$$524 \quad y_t = Y_t - S_t = \mu + \omega X_t + N_t, t = 1, \dots, T \quad (A2)$$

525 The noise  $N_t$  is assumed to be autoregressive of the order of 1 (AR1):

$$526 \quad N_t = \phi N_{t-1} + \epsilon_t \quad (A3)$$

527 where  $\epsilon_t$  is assumed to be random white noise with zero mean and common variance  $\sigma_\epsilon^2$ ,  
528  $\epsilon_t \sim W(0, \sigma_\epsilon^2)$ . The autocorrelations in the noise come from various natural factors.  $\phi$  is  
529 determined as the autocorrelation coefficient of the AR1 process after removing from  $y_t$  a  
530 linear trend component obtained by regressing  $y_t$  to time using a simple weighted linear least  
531 squares method (i.e., neglecting the AR1). The all-sky  $\phi$  is shown in Figure A2a.

532 The variance of the noise  $N_t$  can also be determined from the detrended  $y_t$  time  
533 series:

$$534 \quad \begin{aligned} \sigma_N^2 &= Cov(N_t, N_t) = Cov(\phi N_{t-1} + \epsilon_t, \phi N_{t-1} + \epsilon_t) \\ &= \phi^2 Cov(N_{t-1}, N_{t-1}) + Cov(\epsilon_t, \epsilon_t) \\ &= \phi^2 \sigma_N^2 + \sigma_\epsilon^2 \end{aligned} \quad (A4)$$

535 Thus,

$$536 \quad \sigma_N^2 = \frac{\sigma_\epsilon^2}{1 - \phi^2} \quad (A5)$$

### 537 A.2 Trend estimation with weights

538 Given  $\phi$ , to obtain the trend estimation, we consider a transformed model:

$$\begin{aligned}
y_t^* &= y_t - \phi y_{t-1} \\
&= \mu(1 - \phi) + \omega(X_t - \phi X_{t-1}) + \epsilon_t \\
&= \mu(1 - \phi) + \omega \left[ \frac{t - \phi(t-1)}{12} \right] + \epsilon_t \\
&= \mu(1 - \phi) + \frac{\omega\phi}{12} + \frac{\omega(1-\phi)t}{12} + \epsilon_t \\
&= \mu^* + \omega t^* + \epsilon_t
\end{aligned}
\tag{A6}$$

539

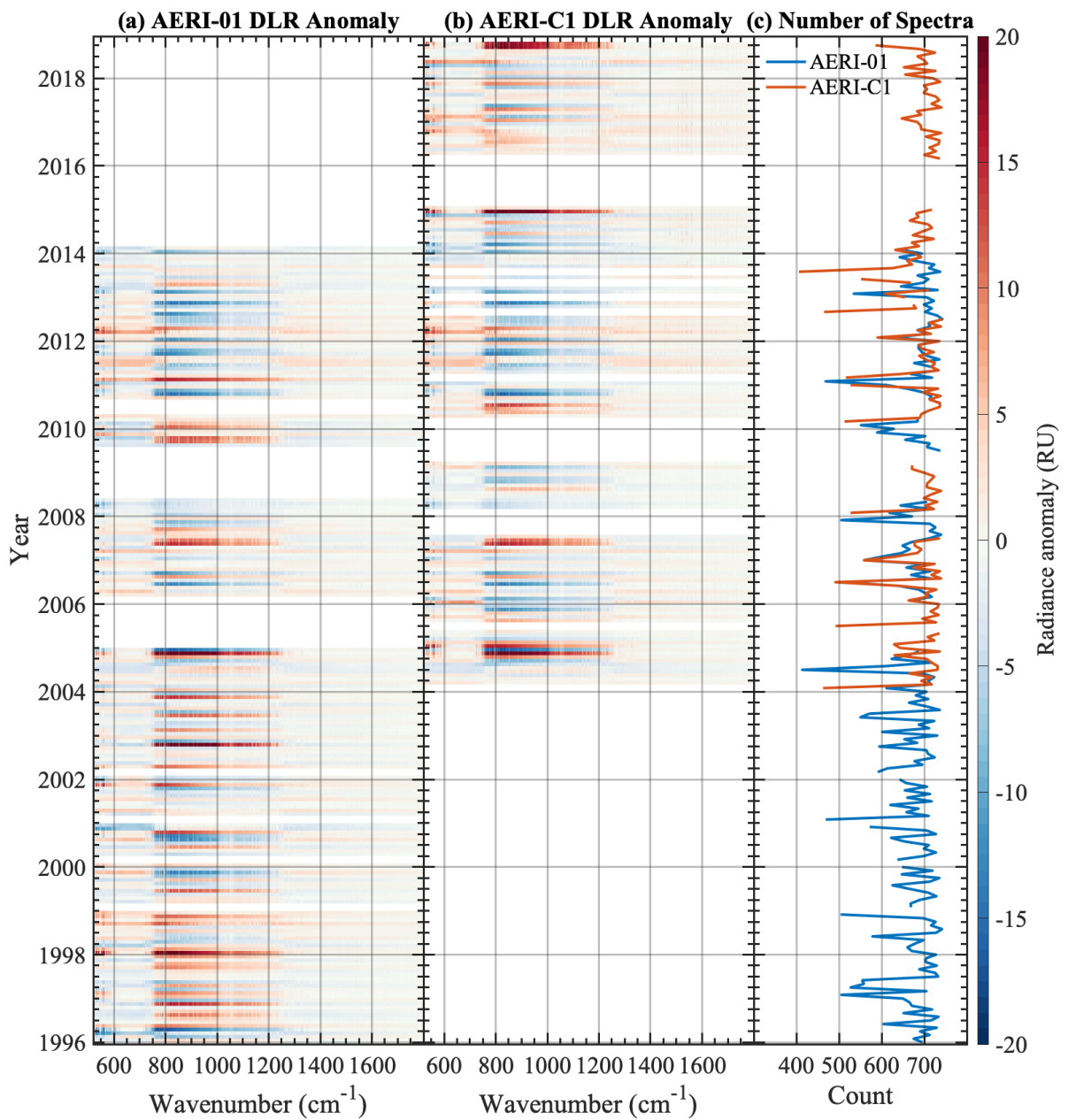
540

where  $\mu^* = \mu(1 - \phi) + \frac{\omega\phi}{12}$  and  $t^* = \frac{(1-\phi)t}{12}$ . Thus, in the transformed model, the noise term  $N_t$  has been removed.

541

542

The transformed DLR  $y_t^*$  is shown in Figure A1.



543

544 **Figure A1.** Transformed monthly anomaly of AERI-observed DLR spectra based on  
 545 Equation (A6) and hourly spectra count in each month.

546 According to the weighted least square estimation:

$$547 \quad \hat{\omega} = \frac{\sum_{t=1}^T W_t(t^* - \bar{t}^*)y_t^*}{\sum_{t=1}^T W_t(t^* - \bar{t}^*)^2} = \frac{\sum_{t=1}^T W_t(t - \bar{t})y_t^*}{\frac{1-\phi}{12} \sum_{t=1}^T W_t(t - \bar{t})^2} \quad (A7)$$

548 where  $W_t$  represents the weights determined according to Equation (4),  $\overline{y_t^*} = \frac{\sum_{t=1}^T W_t y_t^*}{\sum_{t=1}^T W_t}$ ,  $\bar{t}^* =$   
 549  $\frac{\sum_{t=1}^T W_t t^*}{\sum_{t=1}^T W_t}$ , and  $\bar{t} = \frac{\sum_{t=1}^T W_t t}{\sum_{t=1}^T W_t}$ .

550 The variance of the estimated  $\omega$ :

$$551 \quad \sigma_{\hat{\omega}}^2 = Var(\hat{\omega}) = Var \left[ \frac{\sum_{t=1}^T W_t(t - \bar{t})y_t^*}{\frac{1-\phi}{12} \sum_{t=1}^T W_t(t - \bar{t})^2} \right] = \frac{Var \left[ \sum_{t=1}^T W_t(t - \bar{t})y_t^* \right]}{\left( \frac{1-\phi}{12} \right)^2 \left[ \sum_{t=1}^T W_t(t - \bar{t})^2 \right]^2}$$

$$552 \quad = \frac{Var \left[ \sum_{t=1}^T W_t(t - \bar{t})\epsilon_t \right]}{\left( \frac{1-\phi}{12} \right)^2 \left[ \sum_{t=1}^T W_t(t - \bar{t})^2 \right]^2} = \frac{\sum_{t=1}^T [Var[W_t(t - \bar{t})\epsilon_t]]}{\left( \frac{1-\phi}{12} \right)^2 \left[ \sum_{t=1}^T W_t(t - \bar{t})^2 \right]^2}$$

$$553 \quad = \frac{Var(\epsilon_t) \sum_{t=1}^T W_t^2(t - \bar{t})^2}{\left( \frac{1-\phi}{12} \right)^2 \left[ \sum_{t=1}^T W_t(t - \bar{t})^2 \right]^2} = \frac{\sigma_{\epsilon}^2 \sum_{t=1}^T W_t^2(t - \bar{t})^2}{\left( \frac{1-\phi}{12} \right)^2 \left[ \sum_{t=1}^T W_t(t - \bar{t})^2 \right]^2} \quad (A8)$$

$$554 \quad \sigma_{\hat{\omega}} = \frac{\sigma_{\epsilon}}{\frac{1-\phi}{12}} \frac{\sqrt{\sum_{t=1}^T W_t^2(t - \bar{t})^2}}{\sum_{t=1}^T W_t(t - \bar{t})^2} = \sigma_N g(T, \phi, W) \quad (A9)$$

555 In Equation (A9),  $g$  is a function of  $T$ ,  $\phi$ , and  $W$  with the explicit expression shown in  
 556 Equation (A10).

$$557 \quad g(T, \phi, W) = 12 \frac{\sqrt{1+\phi}}{\sqrt{1-\phi}} \frac{\sqrt{\sum_{t=1}^T W_t^2(t - \bar{t})^2}}{\sum_{t=1}^T W_t(t - \bar{t})^2} \quad (A10)$$

558 Thus,

$$559 \quad \sigma_{\hat{\omega}} = 12 \sigma_N \frac{\sqrt{1+\phi}}{\sqrt{1-\phi}} \frac{\sqrt{\sum_{t=1}^T W_t^2(t - \bar{t})^2}}{\sum_{t=1}^T W_t(t - \bar{t})^2} \quad (A11)$$

560 From equation (A11), we conclude that the trend uncertainty is affected by the  
 561 length of the available data, the natural variability in the data, the autocorrelation of the data,  
 562 and the derived weights.

563 A.3 Effect of measurement error

564 When we consider the instrumentation errors  $e_t$  in the measurements, Equation A2  
565 becomes:

$$566 \quad y_t = \mu + \omega X_t + N_t + e_t, t = 1, \dots, T \quad (A12)$$

567  $e_t$  is considered to be white noise with zero mean and common variance  $\sigma_e^2$ ,  
568  $e_t \sim W(0, \sigma_e^2)$ , and is considered independent of  $N_t$  because  $N_t$  originates from unobserved  
569 or unsuspected atmospheric factors, while  $e_t$  comes from the instrument itself.

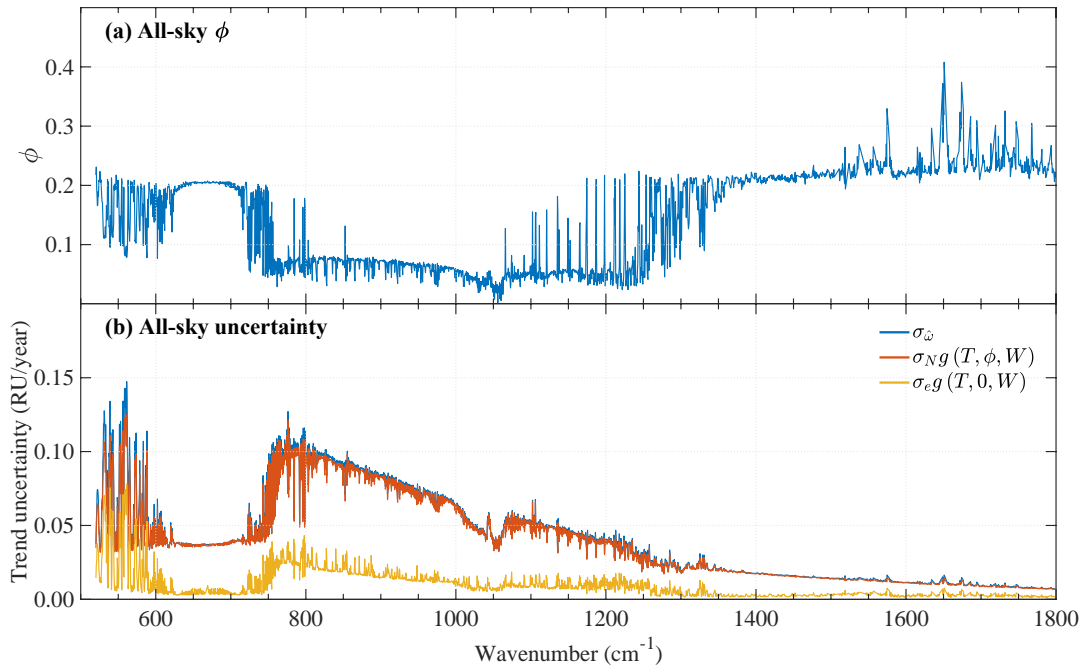
570 In this case, the variance of noise comes from two parts:

$$571 \quad \sigma^2 = \sigma_N^2 + \sigma_e^2 \quad (A13)$$

572 Similar to the derivation in Equation (A9), the variance of the estimated trend  
573 magnitude is:

$$574 \quad \begin{aligned} \sigma_{\hat{\omega}}^2 &= \sigma_N^2 g^2(T, \phi, W) + \sigma_e^2 g^2(T, 0, W) \\ &= \sigma_N^2 \frac{1 + \phi}{1 - \phi} \frac{144 \sum_{t=1}^T W_t^2 (t - \bar{t})^2}{\left[ \sum_{t=1}^T W_t (t - \bar{t})^2 \right]^2} + \sigma_e^2 \frac{144 \sum_{t=1}^T W_t^2 (t - \bar{t})^2}{\left[ \sum_{t=1}^T W_t (t - \bar{t})^2 \right]^2} \\ &= \left( \sigma_N^2 \frac{1 + \phi}{1 - \phi} + \sigma_e^2 \right) \frac{144 \sum_{t=1}^T W_t^2 (t - \bar{t})^2}{\left[ \sum_{t=1}^T W_t (t - \bar{t})^2 \right]^2} \end{aligned} \quad (A14)$$

575 The uncertainty of the all-sky radiance trend magnitude caused by the natural  
576 variability and the measurement error are shown in Figure A2b.



577 **Figure A2.** Parameters concerning the radiance trends. (a) The all-sky autocorrelation  
578 coefficient based on an AR1 process; (b) All-sky DLR trend uncertainty decomposition based  
579 on Equation (A14). The blue line represents the total all-sky trend magnitude uncertainty,  
580 while the orange and yellow lines represent the all-sky trend magnitude uncertainty arising  
581 from natural climate variability and measurement error respectively.  
582

## 583 A.4 Time to detect the trend

584 The trend detection  $\omega$  is judged to be real or significantly different from zero at the  
 585 95% level if  $|\hat{\omega}| > 2\sigma_{\hat{\omega}}$ .  $\hat{\omega}$  is approximately normally distributed, so  $z = \frac{\hat{\omega}-\omega}{\sigma_{\hat{\omega}}}$  follows a  
 586 standard normal distribution.

$$587 \quad Pr(|\hat{\omega}| > 2\sigma_{\hat{\omega}}) = Pr\left(z > 2 - \frac{\omega}{\sigma_{\hat{\omega}}}\right) \quad (A15)$$

588 To detect a real trend of specified magnitude  $|\omega|$ , with probability of 90%: requires  
 589 that  $2 - \frac{\omega}{\sigma_{\hat{\omega}}} < -1.3 \Rightarrow \omega > 3.3\sigma_{\hat{\omega}}$ .

590 Thus, the number of years  $n^*$  of data required to detect the trend  $\hat{\omega}$  which is  
 591 determined based on 23-year data, assuming that the trend and noise levels do not change  
 592 relative to the 23-year period, is

$$593 \quad n^* \approx \frac{3.3\sigma_{\hat{\omega}}}{|\hat{\omega}|} \times 23 \text{ years} \quad (A16)$$

594 We note that the T2D estimation is different from ascertaining whether the trend  
 595 magnitude measured from data is significantly different from zero. Hence, although in some  
 596 channels the trend magnitude is assessed to be "significant", the estimated T2D may be  
 597 longer than the record length (23 years). This is because when estimating T2D we recognize  
 598 that the measured time series is one of the many possible realizations that, although governed  
 599 by the same physical processes and thus of the same true trend, may not render the same  
 600 trend magnitude in the data. This explains why the factor (3.3) used in the T2D estimation is  
 601 different from that (2.0) used in the trend significance test.

602

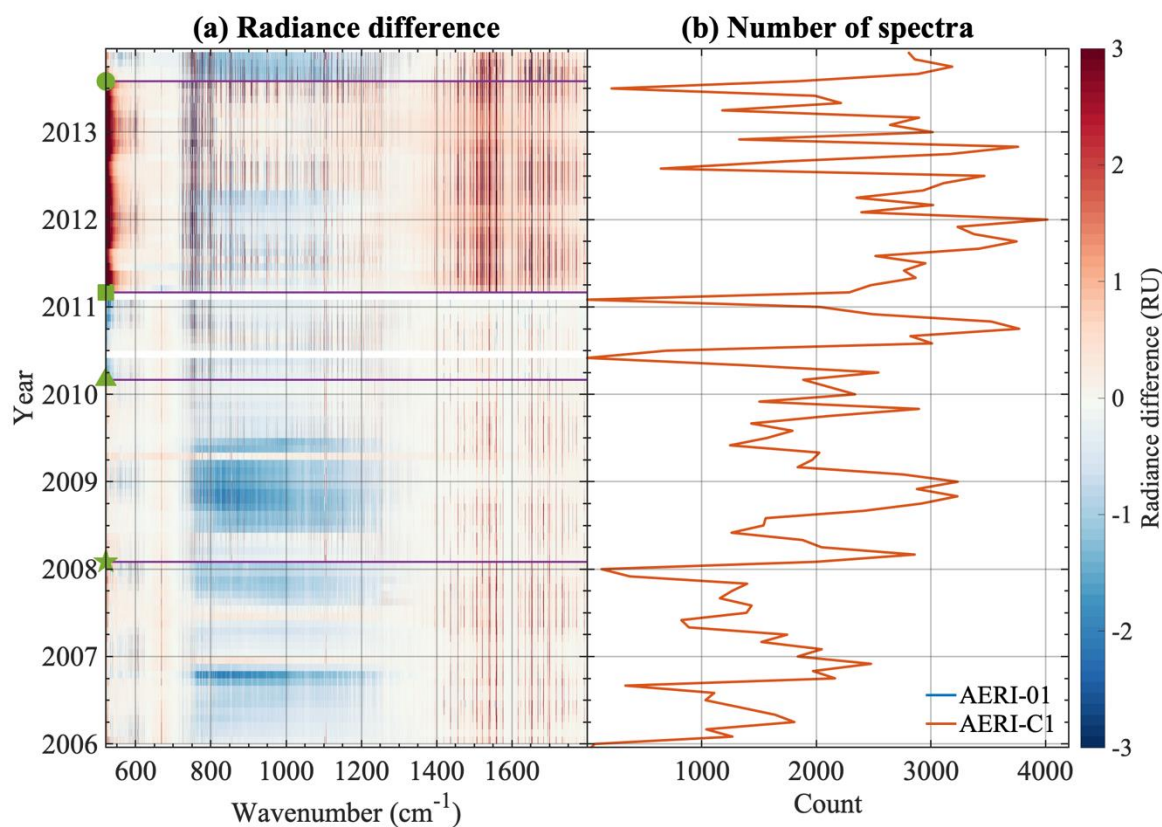
603 **Appendix B: Homogenization of the two AERI records**

## 604 B.1 Comparison between the two AERIs

605 During the overlapping observation period, the all sky monthly mean radiance  
 606 difference between AERI-01 and AERI-C1 is shown in Figure B1. Since these two  
 607 instruments have different sampling frequency, the AERI-C1 spectra are averaged to match  
 608 the sampling of AERI-01 spectra before the comparison. From Figure B1a, there are  
 609 noticeable discrepancies between the AERI-01 and AERI-C1 observations. Because of the  
 610 different sampling frequency, the two AERIs have random errors of different amplitudes  
 611 (Turner et al., 2006). However, we find that removing the random errors using the principal  
 612 component analysis following Turner et al. (2006) has little impact on the discrepancies (not  
 613 shown). We find that in more than 20% of the AERI channels in the spectral range from 700  
 614 to 1300  $\text{cm}^{-1}$  and for more than 12% of the overlapping observational months, the radiance  
 615 difference between two AERIs is larger than the documented absolute calibration uncertainty  
 616 (Knuteson et al., 2004a).

617 For the AERI-C1 data stream, multiple instruments were used. All these transitions  
 618 can be seen in Figure B1a as either subtle changes or obvious differences. First, the transition  
 619 from AERI-04 to AERI-05 happened in September 2009, which caused subtle changes and is  
 620 labelled by the green star in Figure B1a. These AERIs were among the several AERIs  
 621 constructed by the University of Wisconsin – Madison for the ARM program. Next, in March  
 622 2010, the instrument changed from AERI-05 to AERI-06, which is labelled by the green  
 623 triangle in Figure B1a. Then, the transition from AERI-06 to AERI-106 happened in March  
 624 2011, which caused more noticeable changes and is labelled by the green square in Figure

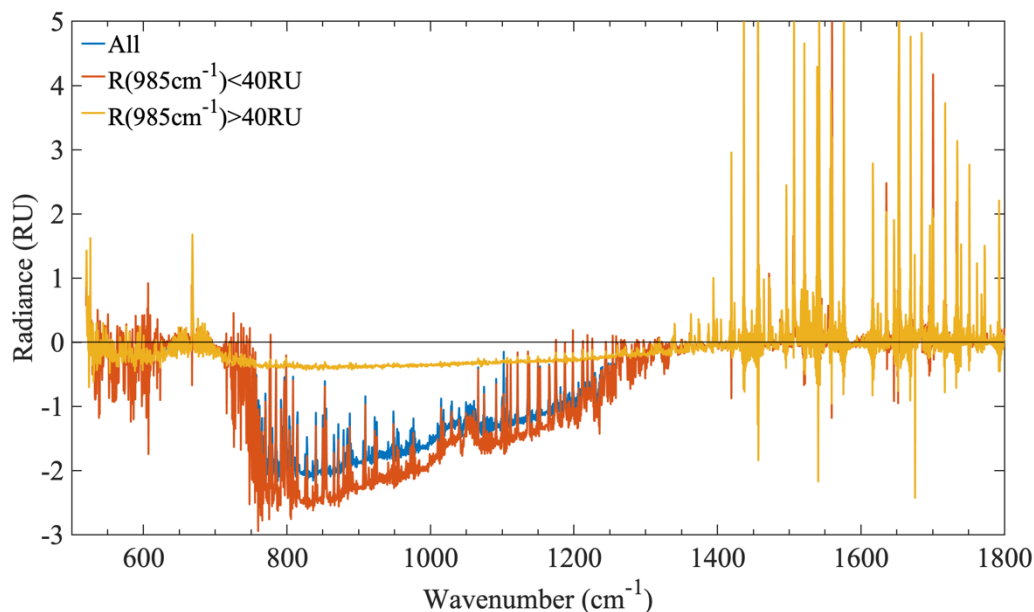
625 B1a. At this point, the AERI technology was licensed to a commercial vendor, and their units  
 626 are now characterized by a three-digit number. So AERI-106 is the 6<sup>th</sup> unit constructed by the  
 627 vendor. AERI-106 operated until July 2013, when it was replaced with the AERI-108 which  
 628 has operated at the SGP site since then. We find that the radiance differences between all of  
 629 these “AERI-C1” instruments and the AERI-01 have unique spectral signatures.



630

631 **Figure B1.** (a) The monthly mean DLR difference between AERI-C1 and AERI-01 (AERI-  
 632 C1 – AERI-01). The green symbols indicate AERI-C1 instrument transitions; (b) Number of  
 633 8-min spectra for each month (the counts are identical after AERI-C1 spectra are resampled  
 634 to match AERI-01).

635 When separating the measured spectra by different sky conditions, we find that the  
 636 prominent difference between the two AERIs in the window band mainly comes from  
 637 relatively clear sky conditions. Figure B2 shows the monthly mean radiance difference for  
 638 different sky conditions in October 2006 as an example. Here the DLR at 985 cm<sup>-1</sup> is used to  
 639 classify the sky to be relatively clear or optically thin clouds (< 40 RU) or relatively cloudy  
 640 (> 40 RU). We chose 40 RU based on the threshold that Turner and Gero (2011) used to  
 641 classify cloudy sky to be thin or thick clouds scenes.



642

643 **Figure B2.** The monthly mean DLR difference between AERI-C1 and AERI-01 (AERI-C1 –  
 644 AERI-01) for different sky conditions in October 2006. See text for details.

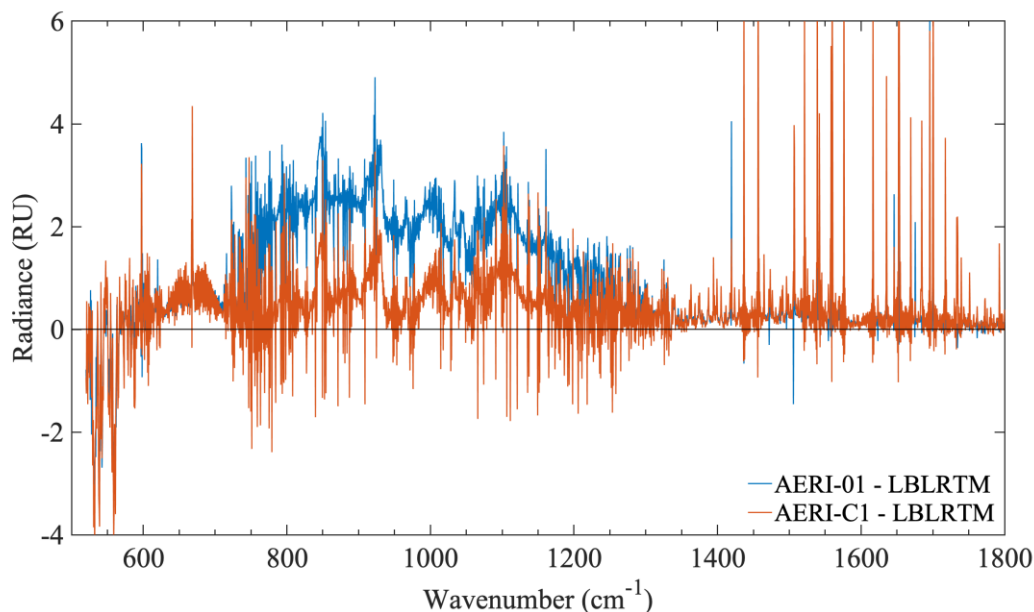
645 We examined various instrumental parameters recorded with AERI measurements,  
 646 including calibration blackbody temperatures and instrument responsivity, but found that no  
 647 instrumental parameter explains the radiance difference between the two AERIs. It is possible  
 648 that an unknown obstruction was partially in the FOV of one of the AERIs (e.g., unit AERI-  
 649 106), such as what was experienced with an early AERI at the SGP site (Knuteson et al.,  
 650 1999).

## 651 B.2 Clear-sky LBLRTM simulations

652 Since the differences between two AERIs mainly come from relatively clear sky  
 653 scenes, we use clear sky synthetic spectra simulated by the LBLRTM as a metric to  
 654 distinguish their relative accuracies. Here we use the classical backpropagation gradient-  
 655 descent classification algorithm mentioned in Subsection 2.2 to select clear-sky spectra. To  
 656 ensure the case is clear, we set the algorithm threshold to be 0.8, which means the probability  
 657 of the sky being clear is at least 0.8.

658 After matching all datasets, including radiosondes and gas concentrations at SGP  
 659 mentioned in section 2.3 to select atmospheric profiles, clear sky synthetic spectra are  
 660 obtained during the overlapping observational period. For each month, about 70 DLR spectra  
 661 are simulated on average. The LBLRTM simulation is validated based on the test in Feldman  
 662 et al. (2015). We chose the same time slices selected in Feldman et al. (2015) to simulate the  
 663 DLR spectrum and we can achieve similar radiative closures between observation and  
 664 simulation.





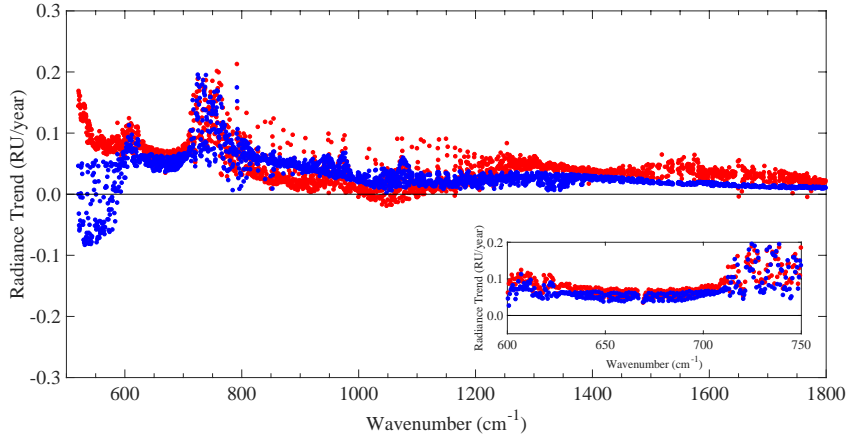
665

666 **Figure B3.** The clear-sky monthly mean DLR difference between AERI-observations and  
 667 LBLRTM simulations in October 2006.

668 We originally used the ozone concentration profile from the Modern-Era  
 669 Retrospective analysis for Research and Applications Version 2 (MERRA-2, Gelaro et al.,  
 670 2017) in simulating the synthetic spectra. A relatively poorer radiance closure between  
 671 AERI-observations and LBLRTM simulations was found in the ozone absorption band near  
 672  $1040\text{ cm}^{-1}$  (not shown). By comparing the in-situ measurements at SGP (available only at  
 673 limited times), we find that this is due to poor representation of the near-surface (and hence  
 674 lower tropospheric) ozone concentration in the MERRA-2 dataset. To address this issue, we  
 675 vertically scale the ozone profile uniformly to achieve an improved radiance closure in the  
 676 ozone band as exemplified by Figure B3 (AERI-C1 line); however, this change to the ozone  
 677 absorption region between  $1040\text{--}1140\text{ cm}^{-1}$  has little impact on the all-sky radiance trend  
 678 detected in Figure 5.

679 As demonstrated in Figure B3, we find that the AERI-C1 is generally in better  
 680 agreement with LBLRTM simulations than AERI-01, especially in the window band. The  
 681 radiance difference in each channel is used to weight the spectra of AERI-01 and AERI-C1,  
 682 according to Equation (2), allowing us to develop an integrated record of monthly mean DLR  
 683 spectra from the two instruments.

684 Figure B4 shows the comparison between LBLRTM simulated clear-sky DLR trends  
 685 (blue dots) and AERI-observed clear-sky DLR trends (red dots) over the 23-year period. The  
 686 clear-sky DLR trends using simulated clear-sky DLR values are similar to the clear-sky DLR  
 687 trends using AERI-observations indicating the reliability of the simulated DLR long-term  
 688 record.



689

690

691

692

**Figure B4.** Comparison between LBLRTM simulated clear-sky DLR trends (blue dots) and AERI-observed clear-sky DLR trends (red dots) over the 23-year period. The inset shows the zoomed-in comparison in the CO<sub>2</sub> absorption band.

693

694

**Appendix C: Comparison of the estimations of time to detect radiance trends**

695

696

697

Leroy et al. (2008) proposed a formula (hereinafter referred to as the Leroy method) to calculate the minimum time to detect (T2D) a trend. T2D calculated using Equation (6) (hereinafter referred to as the Liu method) is longer than using the Leroy method.

698

699

700

701

702

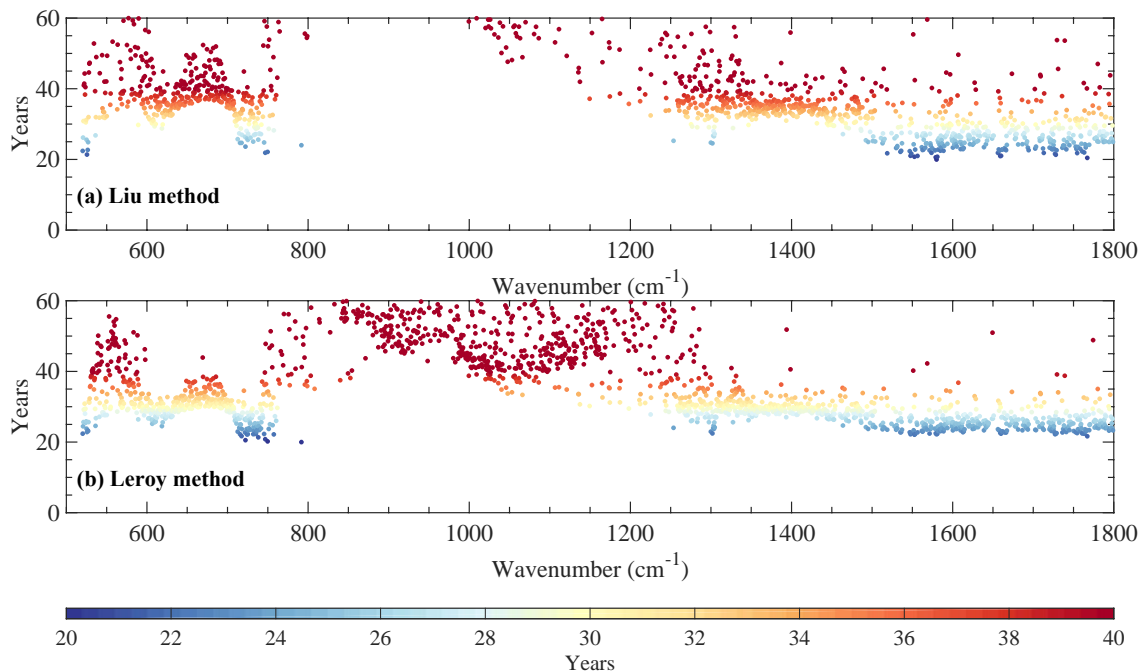
Figure C1 shows the time to detect (T2D) radiance trends at 90% significance level in different AERI channels using Liu the method and the Leroy method respectively. The signal-to-noise ratio  $s$  in Equation (11) of Leroy et al. (2008) is set to be 3.3 in order to be consistent with our derivation in Appendix A4; the terms  $\sigma_{var}$  and  $\sigma_{mean}$  in this equation correspond to  $\sigma_N$  and  $\sigma_e$  in Equation (5) respectively.

703

704

705

The correlation coefficient between T2Ds obtained from the two methods is 0.93. T2D calculated using the Liu method is generally longer than that calculated using the Leroy method by 10 years when T2D is 40 years, and by 45 years when T2D is 100 years.



706

707 **Figure C1.** Trend detectability comparison between using (a) the Liu method and (b) the  
708 Leroy method.

709

710 **References**

711 Brindley, H., & Bantges, R. (2016). The spectral signature of recent climate change. *Current*  
712 *Climate Change Reports*, 2(3), 112-126.

713

714 Clough, S. A., Shephard, M. W., Mlawer, E. J., Delamere, J. S., Iacono, M. J., Cady-Pereira,  
715 K., Boukabara, S., & Brown, P. D. (2005). Atmospheric radiative transfer modeling: a  
716 summary of the AER codes. *Journal of Quantitative Spectroscopy and Radiative*  
717 *Transfer*, 91(2), 233-244. <https://doi.org/10.1016/j.jqsrt.2004.05.058>

718

719 Cunningham, P., & Delany, S. J. (2020). k-Nearest neighbour classifiers: (with Python  
720 examples). *arXiv preprint arXiv:2004.04523*.

721

722 Feldman, D. R., Collins, W. D., Gero, P. J., Torn, M. S., Mlawer, E. J., & Shippert, T. R.  
723 (2015, Mar 19). Observational determination of surface radiative forcing by CO<sub>2</sub>  
724 from 2000 to 2010. *Nature*, 519(7543), 339-343. <https://doi.org/10.1038/nature14240>

725

726 Gelaro, R., McCarty, W., Suárez, M. J., Todling, R., Molod, A., Takacs, L., Randles, C. A.,  
727 Darmenov, A., Bosilovich, M. G., & Reichle, R. (2017). The modern-era retrospective  
728 analysis for research and applications, version 2 (MERRA-2). *Journal of Climate*,  
729 30(14), 5419-5454.

730

731 Gero, P. J., & Turner, D. D. (2011). Long-Term Trends in Downwelling Spectral Infrared  
732 Radiance over the U.S. Southern Great Plains. *Journal of Climate*, 24(18), 4831-4843.  
733 <https://doi.org/10.1175/2011jcli4210.1>

734

735 Harries, J. E., Brindley, H. E., Sagoo, P. J., & Bantges, R. J. (2001). Increases in greenhouse  
736 forcing inferred from the outgoing longwave radiation spectra of the Earth in 1970  
737 and 1997. *Nature*, 410(6826), 355-357.

738

739 Hersbach, H., Bell, B., Berrisford, P., Hirahara, S., Horányi, A., Muñoz-Sabater, J., Nicolas,  
740 J., Peubey, C., Radu, R., & Schepers, D. (2020). The ERA5 global reanalysis.

- 741 *Quarterly Journal of the Royal Meteorological Society*, 146(730), 1999-2049.  
742
- 743 Holdridge D. (2020). Balloon-Borne Sounding System (SONDE) Instrument Handbook.  
744 Ed. by Robert Stafford, U.S. Department of Energy. DOE/SC-ARM/TR-029.  
745
- 746 Huang, Y. (2013). A simulated climatology of spectrally decomposed atmospheric infrared  
747 radiation. *Journal of Climate*, 26(5), 1702-1715.  
748
- 749 Huang, Y., Chou, G., Xie, Y., & Souldard, N. (2019). Radiative control of the interannual  
750 variability of arctic sea ice. *Geophysical Research Letters*, 46(16), 9899-9908.  
751
- 752 Huang, Y., Leroy, S. S., & Anderson, J. G. (2010). Determining longwave forcing and  
753 feedback using infrared spectra and GNSS radio occultation. *Journal of Climate*,  
754 23(22), 6027-6035.  
755
- 756 Huang, Y., & Ramaswamy, V. (2009). Evolution and Trend of the Outgoing Longwave  
757 Radiation Spectrum. *Journal of Climate*, 22(17), 4637-4651.  
758 <https://doi.org/10.1175/2009jcli2874.1>  
759
- 760 Huang, Y., Ramaswamy, V., Huang, X., Fu, Q., & Bardeen, C. (2007). A strict test in climate  
761 modeling with spectrally resolved radiances: GCM simulation versus AIRS  
762 observations. *Geophysical Research Letters*, 34(24).  
763 <https://doi.org/10.1029/2007gl031409>  
764
- 765 Huang, Y., Ramaswamy, V., & Soden, B. (2007). An investigation of the sensitivity of the  
766 clear-sky outgoing longwave radiation to atmospheric temperature and water vapor.  
767 *Journal of Geophysical Research*, 112(D5). <https://doi.org/10.1029/2005jd006906>  
768
- 769 Jacobson, A. R., Schuldt, K. N., Miller, J. B., Oda, T., Tans, P., Arlyn, A., Mund, J., Ott, L.,  
770 Collatz, G. J., Aalto, T., Afshar, S., Aikin, K., Aoki, S., Apadula, F., Baier, B.,  
771 Bergamaschi, P., Beyersdorf, A., Biraud, S. C., Bollenbacher, A., Bowling, D.,  
772 Brailsford, G., Abshire, J. B., Chen, G., Huilin, C., Lukasz, C., Sites, C., Colomb, A.,  
773 Conil, S., Cox, A., Cristofanelli, P., Cuevas, E., Curcoll, R., Sloop, C. D., Davis, K.,

774 Wekker, S. D., Delmotte, M., DiGangi, J. P., Dlugokencky, E., Ehleringer, J., Elkins,  
775 J. W., Emmenegger, L., Fischer, M. L., Forster, G., Frumau, A., Galkowski, M., Gatti,  
776 L. V., Gloor, E., Griffis, T., Hammer, S., Haszpra, L., Hatakka, J., Heliasz, M.,  
777 Hensen, A., Hermanssen, O., Hintsa, E., Holst, J., Jaffe, D., Karion, A., Kawa, S. R.,  
778 Keeling, R., Keronen, P., Kolari, P., Kominkova, K., Kort, E., Krummel, P., Kubistin,  
779 D., Labuschagne, C., Langenfelds, R., Laurent, O., Laurila, T., Lauvaux, T., Law, B.,  
780 Lee, J., Lehner, I., Leuenberger, M., Levin, I., Levula, J., Lin, J., Lindauer, M., Loh,  
781 Z., Lopez, M., Luijkx, I. T., Myhre, C. L., Machida, T., Mammarella, I., Manca, G.,  
782 Manning, A., Manning, A., Marek, M. V., Marklund, P., Martin, M. Y., Matsueda, H.,  
783 McKain, K., Meijer, H., Meinhardt, F., Miles, N., Miller, C. E., Mölder, M., Montzka,  
784 S., Moore, F., Josep-Anton, M., Morimoto, S., Munger, B., Jaroslaw, N., Newman, S.,  
785 Nichol, S., Niwa, Y., O'Doherty, S., Mikael, O.-L., Paplawsky, B., Peischl, J., Peltola,  
786 O., Jean-Marc, P., Piper, S., Plass-Dölmer, C., Ramonet, M., Reyes-Sanchez, E.,  
787 Richardson, S., Riris, H., Ryerson, T., Saito, K., Sargent, M., Sasakawa, M., Sawa, Y.,  
788 Say, D., Scheeren, B., Schmidt, M., Schmidt, A., Schumacher, M., Shepson, P.,  
789 Shook, M., Stanley, K., Steinbacher, M., Stephens, B., Sweeney, C., Thoning, K.,  
790 Torn, M., Turnbull, J., Tørseth, K., Bulk, P. V. D., Dinter, D. V., Vermeulen, A.,  
791 Viner, B., Vitkova, G., Walker, S., Weyrauch, D., Wofsy, S., Worthy, D., Dickon, Y., &  
792 Miroslaw, Z. (2020). *CarbonTracker CT2019B*.

793 <https://www.esrl.noaa.gov/gmd/ccgg/carbontracker/CT2019B/>

794  
795 Kapsch, M.-L., Graversen, R. G., Tjernström, M., & Bintanja, R. (2016). The effect of  
796 downwelling longwave and shortwave radiation on Arctic summer sea ice. *Journal of*  
797 *Climate*, 29(3), 1143-1159.

798  
799 Knuteson, R., Revercomb, H., Best, F., Ciganovich, N., Dedecker, R., Dirks, T., Ellington, S.,  
800 Feltz, W., Garcia, R., & Howell, H. (2004a). Atmospheric emitted radiance  
801 interferometer. Part I: Instrument design. *Journal of Atmospheric and Oceanic*  
802 *Technology*, 21(12), 1763-1776.

803  
804 Knuteson, R., Revercomb, H., Best, F., Ciganovich, N., Dedecker, R., Dirks, T., Ellington, S.,  
805 Feltz, W., Garcia, R., & Howell, H. (2004b). Atmospheric emitted radiance  
806 interferometer. Part II: Instrument performance. *Journal of Atmospheric and Oceanic*

807 *Technology*, 21(12), 1777-1789.

808

809 Knuteson, R., Whitney, B., Revercomb, H., & Best, F. (1999). *The history of the University of*  
810 *Wisconsin Atmospheric Emitted Radiance Interferometer (AERI) prototype during the*  
811 *period April 1994 through July 1995*. University of Wisconsin--Madison, Space  
812 Science and Engineering Center.

813

814 Leroy, S. S., Anderson, J. G., & Ohring, G. (2008). Climate signal detection times and  
815 constraints on climate benchmark accuracy requirements. *Journal of Climate*, 21(4),  
816 841-846.

817

818 Liebmann, B., & Smith, C. A. (1996). Description of a complete (interpolated) outgoing  
819 longwave radiation dataset. *Bulletin of the American Meteorological Society*, 77(6),  
820 1275-1277.

821

822 Lubin, D. (1994). The role of the tropical super greenhouse effect in heating the ocean  
823 surface. *Science*, 265(5169), 224-227.

824

825 Palchetti, L., Brindley, H., Bantges, R., Buehler, S., Camy-Peyret, C., Carli, B., Cortesi, U.,  
826 Del Bianco, S., Di Natale, G., & Dinelli, B. (2020). unique far-infrared satellite  
827 observations to better understand how Earth radiates energy to space. *Bulletin of the*  
828 *American Meteorological Society*, 101(12), E2030-E2046.

829

830 Pan, F., Huang, X., Strow, L. L., & Guo, H. (2015). Linear trends and closures of 10-yr  
831 observations of AIRS stratospheric channels. *Journal of Climate*, 28(22), 8939-8950.

832

833 Peters, W., Jacobson, A. R., Sweeney, C., Andrews, A. E., Conway, T. J., Masarie, K., Miller,  
834 J. B., Bruhwiler, L. M., Pétron, G., & Hirsch, A. I. (2007). An atmospheric  
835 perspective on North American carbon dioxide exchange: CarbonTracker.  
836 *Proceedings of the National Academy of Sciences*, 104(48), 18925-18930.

837

838 Revercomb, H. E., Buijs, H., Howell, H. B., LaPorte, D. D., Smith, W. L., & Sromovsky, L.  
839 (1988). Radiometric calibration of IR Fourier transform spectrometers: solution to a

840 problem with the High-Resolution Interferometer Sounder. *Applied Optics*, 27(15),  
841 3210-3218.

842  
843 Revercomb, H. E., Turner, D. D., Tobin, D., Knuteson, R. O., Feltz, W., Barnard, J.,  
844 Bösenberg, J., Clough, S., Cook, D., & Ferrare, R. (2003). The ARM program's water  
845 vapor intensive observation periods: Overview, initial accomplishments, and future  
846 challenges. *Bulletin of the American Meteorological Society*, 84(2), 217-236.

847  
848 Rowe, P. M., Neshyba, S. P., Cox, C. J., & Walden, V. P. (2011). A responsivity-based  
849 criterion for accurate calibration of FTIR emission spectra: identification of in-band  
850 low-responsivity wavenumbers. *Optics express*, 19(7), 5930-5941.

851  
852 Rowe, P. M., Neshyba, S. P., & Walden, V. P. (2011). Responsivity-based criterion for  
853 accurate calibration of FTIR emission spectra: theoretical development and bandwidth  
854 estimation. *Optics express*, 19(6), 5451-5463.

855  
856 Shupe, M. D., & Intrieri, J. M. (2004). Cloud Radiative Forcing of the Arctic Surface: The  
857 Influence of Cloud Properties, Surface Albedo, and Solar Zenith Angle. *Journal of*  
858 *Climate*, 17(3), 616-628. [https://doi.org/10.1175/1520-](https://doi.org/10.1175/1520-0442(2004)017<0616:Crfota>2.0.Co;2)  
859 [0442\(2004\)017<0616:Crfota>2.0.Co;2](https://doi.org/10.1175/1520-0442(2004)017<0616:Crfota>2.0.Co;2)

860  
861 Sokolowsky, G. A., Clothiaux, E. E., Baggett, C. F., Lee, S., Feldstein, S. B., Eloranta, E. W.,  
862 Cadeddu, M. P., Bharadwaj, N., & Johnson, K. L. (2020). Contributions to the Surface  
863 Downwelling Longwave Irradiance during Arctic Winter at Utqiagvik (Barrow),  
864 Alaska. *Journal of Climate*, 33(11), 4555-4577. [https://doi.org/10.1175/jcli-d-18-](https://doi.org/10.1175/jcli-d-18-0876.1)  
865 [0876.1](https://doi.org/10.1175/jcli-d-18-0876.1)

866  
867 Stephens, G. L., Li, J., Wild, M., Clayson, C. A., Loeb, N., Kato, S., L'Ecuyer, T.,  
868 Stackhouse, P. W., Lebsock, M., & Andrews, T. (2012). An update on Earth's energy  
869 balance in light of the latest global observations. *Nature Geoscience*, 5(10), 691-696.  
870 <https://doi.org/10.1038/ngeo1580>

871  
872 Tiao, G. C., Reinsel, G. C., Xu, D., Pedrick, J., Zhu, X., Miller, A., DeLuisi, J., Mateer, C., &

- 873 Wuebbles, D. (1990). Effects of autocorrelation and temporal sampling schemes on  
874 estimates of trend and spatial correlation. *Journal of Geophysical Research:*  
875 *Atmospheres*, 95(D12), 20507-20517.  
876
- 877 Trenberth, K. E., Fasullo, J. T., & Kiehl, J. (2009). Earth's Global Energy Budget. *Bulletin of*  
878 *the American Meteorological Society*, 90(3), 311-324.  
879 <https://doi.org/10.1175/2008bams2634.1>  
880
- 881 Turner, D., Knuteson, R., Revercomb, H., Lo, C., & Dedecker, R. (2006). Noise reduction of  
882 Atmospheric Emitted Radiance Interferometer (AERI) observations using principal  
883 component analysis. *Journal of Atmospheric and Oceanic Technology*, 23(9), 1223-  
884 1238.  
885
- 886 Turner, D. D., & Gero, P. J. (2011). Downwelling 10 $\mu$ m radiance temperature climatology for  
887 the Atmospheric Radiation Measurement Southern Great Plains site. *Journal of*  
888 *Geophysical Research*, 116(D8). <https://doi.org/10.1029/2010jd015135>  
889
- 890 Turner, D. D., Lesht, B. M., Clough, S. A., Liljegren, J. C., Revercomb, H. E., & Tobin, D.  
891 (2003). Dry bias and variability in Vaisala RS80-H radiosondes: The ARM  
892 experience. *Journal of Atmospheric and Oceanic Technology*, 20(1), 117-132.  
893
- 894 Turner, D. D., Tobin, D., Clough, S. A., Brown, P. D., Ellingson, R. G., Mlawer, E. J.,  
895 Knuteson, R. O., Revercomb, H. E., Shippert, T. R., & Smith, W. L. (2004). The QME  
896 AERI LBLRTM: A closure experiment for downwelling high spectral resolution  
897 infrared radiance. *Journal of the Atmospheric Sciences*, 61(22), 2657-2675.  
898
- 899 Wang, J., Cole, H. L., Carlson, D. J., Miller, E. R., Beierle, K., Paukkunen, A., & Laine, T. K.  
900 (2002). Corrections of humidity measurement errors from the Vaisala RS80  
901 radiosonde—Application to TOGA COARE data. *Journal of Atmospheric and*  
902 *Oceanic Technology*, 19(7), 981-1002.  
903
- 904 Weatherhead, E. C., Reinsel, G. C., Tiao, G. C., Meng, X.-L., Choi, D., Cheang, W.-K.,  
905 Keller, T., DeLuisi, J., Wuebbles, D. J., Kerr, J. B., Miller, A. J., Oltmans, S. J., &



- 906 Frederick, J. E. (1998). Factors affecting the detection of trends: Statistical  
907 considerations and applications to environmental data. *Journal of Geophysical*  
908 *Research: Atmospheres*, 103(D14), 17149-17161. <https://doi.org/10.1029/98jd00995>  
909
- 910 Wielicki, B. A., Wong, T., Allan, R. P., Slingo, A., Kiehl, J. T., Soden, B. J., Gordon, C.,  
911 Miller, A. J., Yang, S.-K., & Randall, D. A. (2002). Evidence for large decadal  
912 variability in the tropical mean radiative energy budget. *Science*, 295(5556), 841-844.  
913
- 914 Wild, M., Folini, D., Schär, C., Loeb, N., Dutton, E. G., & König-Langlo, G. (2012). The  
915 global energy balance from a surface perspective. *Climate Dynamics*, 40(11-12),  
916 3107-3134. <https://doi.org/10.1007/s00382-012-1569-8>  
917  
918